IOWA STATE UNIVERSITY
Digital Repository

2015

Development of a robotic platform for maize functional genomics research

Hang Lu
Iowa State University

Development of a robotic platform for maize functional genomics research

by

Hang Lu

A thesis submitted to the graduate faculty

in partial fulfillment of the requirements for the degree of

MASTER OF SCIENCE

Major: Agricultural and Biosystems Engineering

Program of Study Committee:
Lie Tang, Major Professor
Steven A. Whitham
Steven J. Hoff

Iowa State University

Ames, Iowa

2015

DEDICATION

I dedicate this work to my parents and my friend Suxin.

TABLE OF CONTENTS

LIST OF FIGURES

viii

LIST OF TABLES

NOMENCLATURE

GLCM	Gray-Level Co-occurrence Matrix
KNN	K-Nearest Neighbor
NN	Neural Network
VTK	The Visualization Toolkit
PCL	Point Cloud Library
SCMV	Sugarcane Mosaic Virus
TCP	Transmission Control Protocol
SDK	Software Development Kit

ACKNOWLEDGMENTS

ABSTRACT

The food supply requirement of a growing global population leads to an increasing demand for agricultural crops. Without enlarging the current cultivated area, the only way to satisfy the needs of increasing food demand is to improve the yield per acre. Production, fertilization, and choosing productive crops are feasible approaches. How to pick the beneficial genotypes turns out to be a genetic optimization problem, so a biological tool is needed to study the function of crop genes and for the particular purpose of identifying genes important for agronomy traits. Virus-induced gene silencing (VIGS) can be used as such a tool by knocking down gene expression of genes to test their functions.

The use of VIGS and other functional genomics approaches in corn plants has increased the need for determining how to rapidly associate genes with traits. A significant amount of observation, comparison, and data analysis are required for such corn genetic studies. An autonomous maize functional genomics system with the capacity to collect data collection, measure parameters, and identify virus-plants should be developed. This research project established a system combining sensors with customized algorithms that can distinguish a viral infected plant and measure parameters of maize plants.

An industrial robot arm was used to collect data in multiple views with 3D sensors. Hand-eye calibration between a 2D color camera and the robot arm was performed to transform different camera coordinates into arm-based coordinates. TCP socket-based software written in Visual C ++ was developed at both the robot arm side and the PC side to perform behavioral bidirectional real-time communication.

A 3D time-of-flight (ToF) camera was used to reconstruct the corn plant model. The point clouds of corn plants, in different views, were merged into one representation through a homogeneous transform matrix. Functions of a pass-through filter and a statistical outlier removal filter were called from the Point Cloud Library to remove background and random noise. An algorithm for leaf and stem segmentation based on the morphological characteristics of corn plants was developed. A least-squares method was used to fit the skeletons of leaves for computation of parameters such as leaf length and numbers.

After locating the leaf center, the arm is made ready to position the 2D camera for color imaging. Color-based segmentation was applied to pick up a rectangular interest of area on the leaf image. The algorithm computing the Gray-Level Co-occurrence Matrix (GLCM) value of the leaf image was implemented using the OPENCV library. After training, Bayes classification was used to identify the infected corn plant leaf based on GLCM value.

The System User Interface is capable of generating data collection commands, 3D reconstruction, parameter table output, color image acquisition control, specific leaf-probing and infected corn leaf diagnosis. This application was developed under a Qt cross-platform environment with multithreading between tasks, making the interface user-friendly and efficient.

CHAPTER 1. INTRODUCTION: THESIS FORMATTING

1.1 Introduction

By the year 2050, a 70% increase in crop production will be required to meet the needs of a growing global population (Furbank, et al., 2009). Moreover, by 2050 cropland area may decrease slightly in developed countries (Balmford, et al., 2005). Biofuels will also be more widely used, increasing crop production demand (Sticklen, 2007). A feasible approach to satisfy the demand for crops would be to boost yield per acre without enlarging the agricultural area. Genetic optimization is an important tool for discovery of crop strains beneficial to increased production. A phenotyping platform for associating crop genes with traits could assistant humans in improving crop plant yields.

"Phenotype" is defined as "a composite of an organism's observable characteristics or traits, such as its morphology, biochemical or physiological properties, phenology, behavior, and products of behavior." The plant phenotype contains traits of growth, development, tolerance, resistance, yield, and parameters based on observation and measurement. For example, the direct observation and measurement parameters could include leaf traits (Jansen, et al., 2009), fruit characteristics (Brewer, et al., 2006), yield-related traits (Duan, et al., 2011), root morphology (Walter, et al., 2009), biomass (Menzel, et al., 2009), biotic and abiotic stress response (Rao, et al., 2013) and photosynthetic efficiency (Bauriegel, et al., 2011).

Imaging technologies and automation have many applications in screening systems, horticultural production systems, and elsewhere in the food industry supply chain (Arvidsson, et al., 2011). In the past decade, researchers and commercial companies have

developed automated phenotyping systems and applied them to greenhouses and growth chambers. These phenotyping platforms were able not only to research small rosette plants like Arabidopsishalophila (Granier, et al., 2006) but also cereal crops (Deikman, et al., 2012). The most commonly used approach for trait extraction is color segmentation. A plant disease severity estimation platform based on digital photography has been developed to analyze and classify leaf rust levels (Bock, et al., 2010). Thermal imaging has also been used in a phenotyping system for studying plant surface temperature and maize adaption to drought (Jose, et al., 2012). A near-infrared camera technique was utilized in a high-throughput image platform for dissecting the components of crop plant growth and drought responses (Dijun, et al., 2010).

Unlike color images that only include 2D information, a 3D camera technique could provide plant structural information. Currently, four types of 3D sensors: stereo cameras, laser sensors, light field cameras and ToF cameras, are used in phenotyping systems. A stereo imaging system was applied to measurement of the zenith leaf angle distribution of a closed soybean canopy (Biskup et al., 2007). The two major challenges in applying stereo methods in agriculture are mismatch or occlusion problems resulting from a plant's leaf texture and outdoor lighting conditions.

LIDAR scanners are powerful and unsusceptible to sunlight, and an automatic phenotyping system is capable of modeling tomato canopies and extracting leaf inclination angles based on 3D data from a high resolution portable scanning LIDAR (Omasa, et al., 2012). LIDAR sensors have already been applied in large-scale phenotyping systems to estimate the height of trees and structural parameters of forests (Hopkinson, et al., 2004). The

capture processing of a LIDAR scanner requires the plant to be static and unmoving, but it is difficult to satisfy this outdoor condition on windy days.

The 3D light field camera is transformed from a normal camera by placing a micro lens array in front of an image sensor. PhenoBot utilized a 3D light field camera (Raytrix) to measure the phenotypic characteristic, stem thickness, leaf length, and number of flowers per bunch, of tomato plants. The advantage of the Raytrix 3D light field camera is its high resolution, minimal occlusion, and adaptability, but it is very expensive and incapable of calculating depth in real time (Polder, et al., 2013).

The ToF 3D camera is a new-technique product that has become widely used in industrial and entertainment fields over the last several decades. It measures depth by computing the time difference between emitted near-infrared light and reflected light. Microsoft Corporation launched the new generation Kinect Version 2, implemented using a ToF technique, for its X-box game system. Kinect V2 is a composite sensor that includes a color camera, a near-infrared camera and a ToF camera. The PMD Camcube (PDM Tec, Germany) and the SR_4000/4500 series (MESA Imaging AG, Switzerland) are two commonly used ToF cameras. Alenya, et al., (2011) developed a phenotyping system including a ToF camera, a color camera, and an industrial robot arm. This system combined 3D spatial data with a color image and used the color and depth information to segment a single 3D leaf from a whole plant. The limitation of the ToF camera is its low resolution and susceptibility to sunlight, so it is usually used under indoor conditions.

1.2 Research Objectives

The overall goal of this research is to develop an automatic phenotyping system. This system should be capable of measuring corn plant phenotypical parameters, leaf length and stem height, and diagnosing virus-infected plants. The research goal can be divided into three main objectives:

(1) To finish setting up the system with a 3D camera, a color camera, an industrial robot arm, and a complete data collection and background noise removal function. To calibrate the hand-eye relationships among the cameras and the robot arm. To merge multiple views of a corn plant points cloud and visualization of a clear 3D corn model into a user interface.

(2) To segment the leaves and stem and measure plant morphology parameters, leaf length, and stem height. The result table would be displayed in a user-friendly interface.

(3) To use the Gray-level Co-occurrence Matrix (GLCM) method to analyze the texture of leaves and implement Bayes classification to distinguish infected corn plant leaves.

1.3 Thesis Overview

Chapter 2 describes the system set-up, robot, and camera hand-eye calibration, along with the details of transforming point clouds from multiple views into arm-based coordinates. Algorithms for background and noise removal, leaves and stem segmentation, and leaf skull skeleton curve-fitting are also discussed, along with system module design and analysis of results.

Chapter 3 covers the development of the infected plant leaf diagnostic system. It describes the method of computing the color camera viewpoint based on leaf surface normal and centroid point. Chapter 3 also introduces leaf color image segmentation and GLCM value extraction and finally discusses how to set the training set and testing set in Bayes classification.

Chapter 4 provides general conclusions as well as suggestions for future research.

REFERENCES

Alenya, G., B. Dellen, and C. Torras. 2011. 3D modelling of leaves from color and ToF data for robotized plant measuring. In 2011 IEEE International Conference on Robotics and Automation. Shanghai, China: IEEE.

Araus JL, Serret MD, Edmeades GO. 2012. Phenotyping maize for adaptation to drought. Front. Plant Physiol. 3:305

Arvidsson S, Perez-Rodriguez P, Mueller-Roeber B. 2011. A growth phenotyping pipeline for Arabidopsis thaliana integrating image analysis and rosette area modeling for robust quantification of genotype effects. New Phytol. 191:895–907

Balmford, A., Green, Rhys. E. and Scharlemann, J. P. W. (2005), Sparing land for nature: exploring the potential impact of changes in agricultural yield on the area needed for crop production. Global Change Biology, 11: 1594–1605. Doi: 10.1111/j.1365-2486.2005.001035.x

Bauriegel, E.; Giebel, A.; Herppich, W.B. Hyperspectral and chlorophyll fluorescence imaging to analyze the impact of fusarium culmorum on the photosynthetic integrity of infected wheat ears. Sensors 2011, 11, 3765–3779.

Biskup B, Scharr H, Schurr U, Rascher U. 2007. A stereo imaging system for measuring structural parameters of plant canopies. Plant Cell Environ. 30:1299–308

Brewer, M.T.; Lang, L.; Fujimura, K.; Dujmovic, N.; Gray, S.; midrib der Knaap, E. Development of a controlled vocabulary and software application to analyze fruit shape variation in tomato and other plant species. Plant Physiol. 2006, 141, 15–25.

Bock CH, Poole GH, Parker PE, Gottwald TR. 2010. Plant disease severity estimated visually, by digital photography and image analysis, and by hyperspectral imaging. Crit. Rev. Plant Sci. 29:59–107

Deikman J, Petracek M, Heard JE. 2012. Drought tolerance through biotechnology: improving translation from the laboratory to farmers' fields. Curr. Opin. Biotechnol. 23:243–50

Dijun Chen, Kerstin Neumann, Swetlana Friedel, Benjamin Kilian, Ming Chen, Thomas Altmann, and Christian Klukas Dissecting the Phenotypic Components of Crop Plant Growth and Drought Responses Based on High-Throughput Image Analysis Plant Cell tpc.114.129601; First Published on December 11, 2014; doi:10.1105/tpc.114.129601

Duan, L.F.; Yang, W.N.; Huang, C.L.; Liu, Q. A novel machine-vision-based facility for the automatic evaluation of yield-related traits in rice. Plant Methods 2011, 7, doi: 10.1186/1746-4811-7-44.

Furbank, R. T., S. von Caemmerer, J. Sheehy, and G. Edwards. 2009. C-4 rice: A challenge for plant phenomics. Functional Plant Biology 36(10-11):845-856.

Granier C, Aguirrezabal L, Chenu K, Cookson SJ, Dauzat M, et al. 2006. PHENOPSIS, an automated platform for reproducible phenotyping of plant responses to soil water deficit in Arabidopsis thaliana permitted the identification of an accession with low sensitivity to soil water deficit. New Phytol. 169:623–35

Hopkinson, C., L. Chasmer, C. Young-Pow, and P. Treitz. 2004. Assessing forest metrics with a ground-based scanning Lidar. Canadian Journal of Forest Research-Revue Canadienne De Recherché Forestiere 34(3):573-583.

Jansen, M.; Gilmer, F.; Biskup, B.; Nagel, K.A.; Rascher, U.; Fischbach, A.; Briem, S.; Dreissen, G.; Tittmann, S.; Braun, S. Simultaneous phenotyping of leaf growth and chlorophyll fluorescence via growscreen fluoro allows detection of stress tolerance in arabidopsis thaliana and other rosette plants. Funct. Plant Biol. 2009, 36, 902–914.

Menzel, M.I.; Tittmann, S.; Buehler, J.; Preis, S.; Wolters, N.; Jahnke, S.; Walter, A.; Chlubek, A.; Leon, A.; Hermes, N. Non-invasive determination of plant biomass with microwave resonators. Plant Cell Environ. 2009, 32, 368–379.

Omasa K, Hosoi F, Konishi A. 2007. 3D LIDAR imaging for detecting and understanding plant responses and canopy structure. J. Exp. Bot. 58:881–98

Polder G, Lensink D, Veldhuisen B. 2013. PhenoBot – a robot system for phenotyping large tomato plants in the greenhouse using a 3D light field camera. Wageningen UR Glastuinbouw/ENZA Zaden, 2013 Phenodays Meeting, 2013-10-16/ 2013-10-18

Rao, N.K.S.; Laxman, R.H. Phenotyping horticultural crops for abiotic stress tolerance. In Climate-Resilient Horticulture: Adaptation and Mitigation Strategies; Springer: Berlin/Heidelberg, Germany, 2013; pp. 147–157.

Sticklen, M. B. 2007. Feedstock crop genetic engineering for alcohol fuels. Crop Science 47(6):2238-2248.

Wikipedia Phenotype. http://en.wikipedia.org/wiki/Phenotype

Walter, A.; Silk, W.K.; Schurr, U. Environmental effects on spatial and temporal patterns of leaf and root growth. Ann. Rev. Plant Biol. 2009, 60, 279–304.

CHAPTER 2. DEVELOPMENT OF AN AUTOMATIC MAIZE SEEDLING PHENOTYPING PLATFROM USING 3D VISION AND AN INDUSTRIAL ROBOT ARM

2.1 Abstract

Crop breeding plays an important role in modern agriculture, improving plant adaptability and increasing yield. Optimizing genes is the key step in discovery of beneficial genetic traits for increasing crop production. Associating genes and their functions requires a mountain of observation and measurement of the phenotypes, a repetitive and error-prone job if performed manually. An automated seedling phenotyping system aims at replacing manual measurement, reducing the sampling time and increasing the allowable work time. In this research study, we developed an automated maize seedling phenotyping platform based on a ToF camera and an industrial robot arm. A ToF camera is mounted on the end-effector of the robot arm. The arm positions the ToF camera to different viewpoints for acquiring 3D data. A camera-to-arm transformation matrix is calculated from hand-eye calibration and applied to transfer different viewpoints into an arm base coordinate frame. Filters remove the background and noise in the merged seedling point clouds. 3D-to-2D projection and the x-axis pixel density distribution method is used to segment the stem and leaves. Finally, separated leaves are fitted with 3D curves for parameter measurement. This platform was tested on a sample of 60 maize plants at early growth stages (V2~V5).

Keywords: Phenotyping, Maize breeding, 3D reconstruction, Point clouds, robot arm, ToF camera

2.2 Introduction

Breeders and ecologists have been studying plant phenotyping for many years. High-throughput phenotyping for evaluating hundreds of genotypes is routine in plant breeding (Foundation and Mcb, 2011). Ijiri, et al., (2005) developed an application for modeling flowers in 3D. This system could picture the layout of floral components on a flower, helping botanists concisely describe the structure of flowers quickly and easily. Some groups of researchers provided 3D models of rice plants from images and barley plants from 3D sensors. Watanabe, et al., (2005) used a 3D digitizer to measure rice plant structure to specify rice plant architecture and to find suitable functions for describing its 3D growth at all stages. Recently, plant phenotyping has gained more attention because of the development of advanced sensors and robotic data collecting and monitoring methodology. Ulrich, et al., (2011) used 3D LIDAR sensors to develop an application for dealing with detection and segmentation of plants and ground. Their result showed that this application could assist agricultural robots used for localization, mapping and navigation. Yann, et al., (2012) proposed an algorithm based on 3D data to do plant segmentation from a top view. In that experiment, the leaves of yucca and apple trees at different depths could be segmented and distinguished very well.

There are a variety of methods for corn plant phenotype discovery and 3D visualization. Dornbusch, et al., (2007) improved the modeling function of the shape of corn plant's leaves and stems and proposed a new method for function parameterization function from a 3D point cloud of the plants. Although they achieved excellent results, the image cannot be automatically captured, and this approach was not proven to apply to all kinds of corn plants. De Moraes Frasson, et al., (2010) also developed an application to build detailed

three-dimensional digital models of corn plants by using an unmodified commercial digital camera and software. 3D reconstruction of plants is the first step; this provides the morphology and position information, and the goal is to perform operations on the plant (such as probing and cutting of the plant). Aleny`a, et al., (2011) used ToF depth data to perform quadratic surface fitting applied to segmenting plant images. Their result showed that the obtained surface fit well with target leaf and the candidate leaf could be approached by a robot-mounted camera using location information. This work proved that combining dense color data and depth data could provide a good 3D approximation to automatically complete plant measurements.

One potential application is to use the phenotype information for guiding an agricultural or biological robot. Teng, et al., (2011) treated normalized centroid-contour distance as the classification feature for sorting different leaves in their system. Their leaf segmentation and classification system combined 3D information and color character for leaf classification; it is not, however, fully automatic. Klose, et al., (2009) constructed an outdoor automatic plant phenotyping system. They concluded that ToF cameras could also be useful in outdoor field conditions like direct sunlight. Their system could also collect data while moving at a speed of 3.6 km/h, meaning that it could be used in combination with an autonomous field robot.

This research is focused on developing a fully automatic maize seedling phenotyping platform capable of outputting maize seedlings' morphological traits, including number of leaves, leaf length, and stem height.

2.3 Materials and Method

An overview of the platform is shown in Figure 2.1. The system contains a time-of-flight (ToF) camera (SR_4000, MESA Imaging, Switzerland), an industrial robot arm (RV_3SD, Mitsubishi, Japan), and a computer station. After the "Acquire 3D data" button is pressed at the user interface, the system sends commands to the robot arm, including commands to specific positions with various poses to acquire a 3D point cloud from these viewpoints. The point clouds are then transformed and merged into arm base coordinates. The platform performs filtering, stem and leaf segmentation, phenotype output, and visualization.
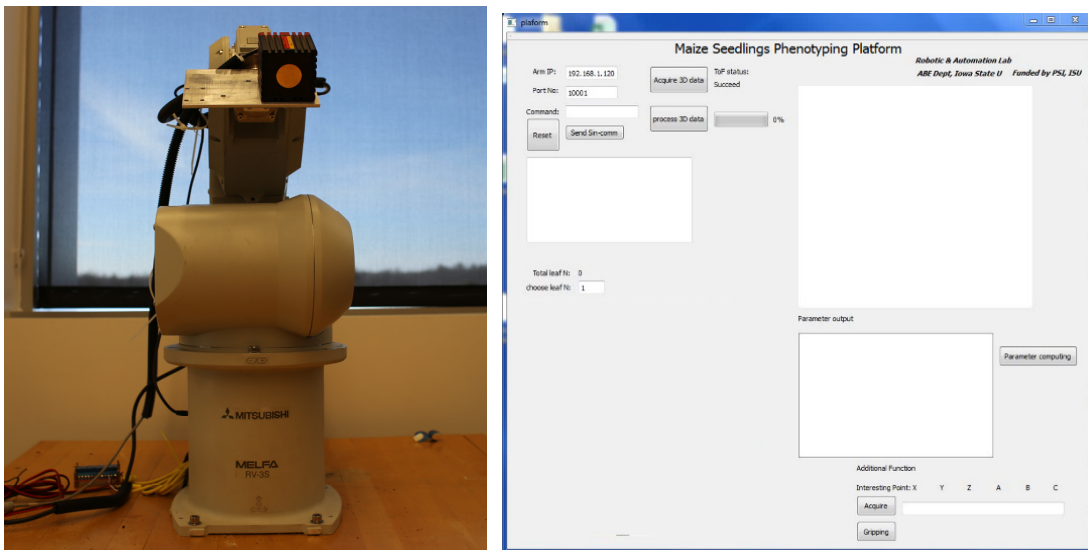
Figure 2.1. Hardware set-up (left) and software interface (right).

2.3.1 Data collection station setup

Figure 2.2 shows how the ToF camera connects to the end-effector of the robot arm. The aluminum mounting bracket (McMaster-Carr, USA) has a 90 degree "L" shape with 5-inch width and ¼-inch depth. It was designed and machined by Manual Mills (Clausing, USA), with 4 holes on one side connecting to the robot arm end-effector, and 3 holes on the other side for fixing the ToF camera.
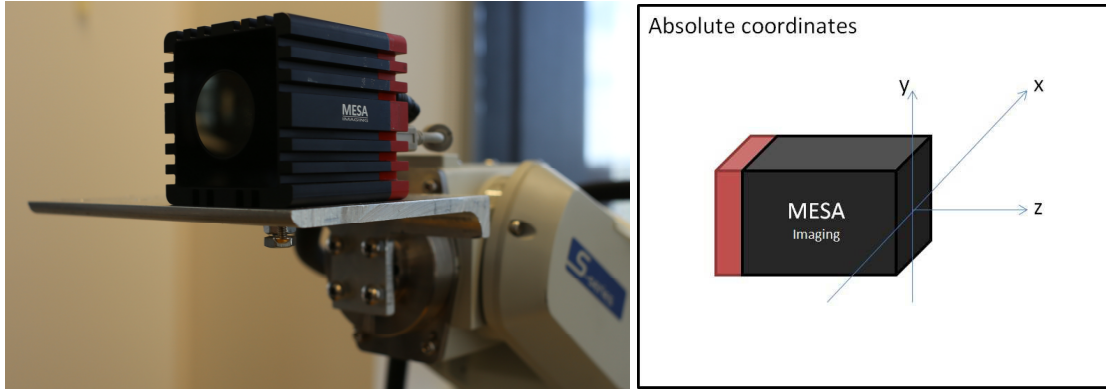
Figure 2.2 *ToF camera mounted on the end-effector of the robot arm (left), the ToF camera coordinate (right, this figure is from the ToF camera manual).*

The ToF camera (Product number: 00400001, MESA imaging, Switzerland) uses a USB communication port and operates at a 30 MHz frequency. The detection range is 0.1 ~ 5.0 m, and the calibrated range is 0.8 ~ 5.0 m. Its absolute accuracy is ± 10 mm and it has less than 0.5 mm/°C drift with temperature. The repeatability of central pixels is around 4 mm and 7 mm (max). The field of view is 43° (h) × 34°. All the parameters mentioned above are tested at 25° (SR_4000 Manual).

The illumination wavelength of this ToF camera is 850 nm and its maximum frame rate is 50 FPS. The pixel array size is 176 (h) × 144 (v). The pixel pitch is 40 μm and the angular resolution is 0.24°. The operating temperature range is +10°C to +50°C (SR_4000 Manual).

2.3.2 Hand-eye transformation matrix

To estimate the 3D position and orientation of the target object related to the robot base coordinate frame, it is essential to know the relationships between the robot end-effector and the robot base, between the camera and the robot end-effector, and between the target object and the camera. The transformation matrix between the robot end-effector and the base frame can be read from the robot controller output without any programming or

computing. The main function of the ToF camera is to output the 3D point clouds that

provide the position and orientation of the target object in the camera coordinate frame. Thus,

the transformation matrix of camera and robot end-effector must be measured or calibrated to

transfer target object position and orientation information to the robot base frame.

2.3.2.1 Dimension method

The accuracy of the Manual Mills machined mounting bracket is ±0.127 mm (±0.005

inch). According to the dimensions and coordinate definition of the ToF camera in the

manual, the original point at the center of the surface and the xyz directions are shown in the

figure 2.2. The transformation matrix from camera xyz coordinate (Figure 2.3) to robot arm

end-effector is calculated and represented as a rotation matrix and a transformation matrix.

$$R_D = \begin{bmatrix} -0.9998, 0.0174, -0.0006 \\ -0.0175, -0.9992, 0.0349 \\ 0.0000, 0.0349, 0.9994 \end{bmatrix} \qquad 2.1$$

$$T_D = \begin{bmatrix} -30.69 \\ -69.03 \\ 120.96 \end{bmatrix}, \text{ where the unit is mm.} \qquad 2.2$$

2.3.2.2 Fully vision-based calibration

In the normal camera calibration, there are two main outputs, i.e., intrinsic and

extrinsic parameters. The intrinsic parameter is used to calibrate lens distortion, while the

extrinsic parameter can be used to associate the camera position with 3D world space.

Vision-based robot hand-eye calibration applies the normal camera calibration extrinsic

parameters and the constant relationship between camera frame and robot end-effector frame.

We used Hand-Eye calibration Toolbox (Christian W, 2006) to calculate the camera to robot

end-effector transformation matrix.
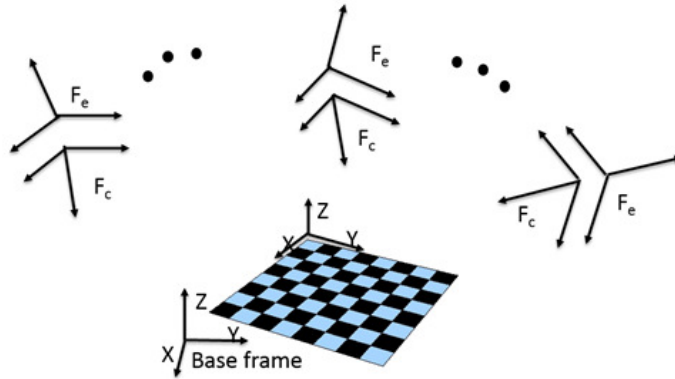
Figure 2.3. *Hand-eye calibration, relationship between camera coordinate and robot arm base coordinate.*

This toolbox would solve 8 set of homogeneous transform equations: AX=XB, where X is the unknown and target matrix. The final result of the camera-related-to-robot end-effector transform matrix had an error of less than 20 mm in each direction.

The toolbox uses the reference pattern method to locate the original location and direction of the coordinate. However, this method becomes less effective when dealing with cameras with lower resolution because the algorithm relies on the accuracy of detection of metric features such as corner and circle center. Larger error is generated when detecting and locating those features in a low-resolution image acquired by a ToF camera; the SR_4000 has a resolution of only 176×144.
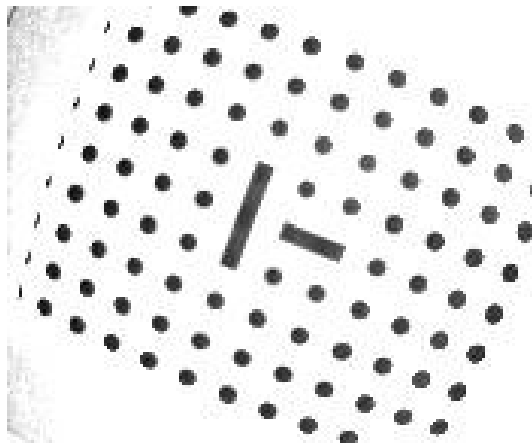
Figure 2.4. *ToF camera amplitude image of a checkerboard with low resolution*

Comparing these two calibration methods, the error of the dimension method is apparently smaller than that of the vision-based ToF camera. Kahn, et al., (2014) reported that there is an approximately 10mm error of SR_4000 2D and 3D image-based hand-eye calibration in their experiment. The dimension method was therefore applied in this project.

2.3.3 System layouts and communication

This system contains four hierarchy modules: a main control module and user interface, a robot arm control module, a ToF camera control module, and a data processing module. The entire system works using multiple threads in which the central module is the main thread and submodules are the child threads; it is written in the Qt development environment using the programing language C++.
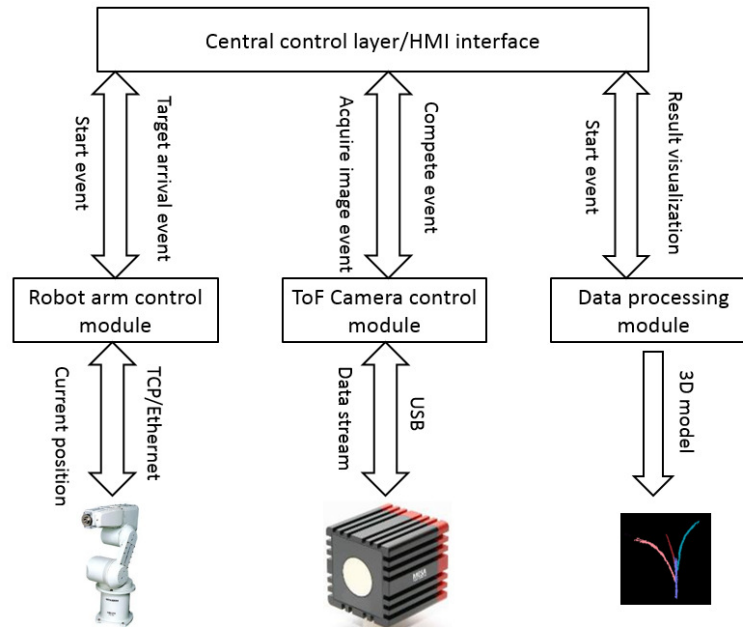
Figure 2.5. *System overview*

2.3.3.1 Main control layer

This main module and interface is a central controller responsible for communication with the robot arm, decision-making for ToF camera action, and triggering data processing and result visualization.

In user operation, the main control layout sends a request instruction to the robot arm control module that would then produce a program for jogging the arm to specific positions. Meanwhile, the robot arm could send its current positon to the main control module in real time. A judgment is made in the main control layer as to whether the arm properly determines the target sampling position. As soon as the arm determines the target locations, the main control module would send a request instruction to the ToF camera control module for acquiring 3D image. When the 3D images of multiple views are ready, the processing module begins filtering, leaf and stem segmentation, and parameter computation. Finally, the phenotype result and 3D reconstruction model are shown as a table and zoom in/out visualization window in the user interface.

The HMI (Human-machine interaction) interface is designed to be user-friendly; it contains robot arm controller IP and port setting, command buttons, camera status-checking, a phenotype parameter output table, and 3D model visualization.

2.3.3.2 Robot arm control module

The Mitsubishi RV3S is an industrial vertical 6-joint robot arm with a maximum speed of 5.5 m/s and 0.02 mm position repeatability. The programming platform, RT ToolBox2 (Mitsubishi, Japan), is an independent software package with its own uniform robot programming language. It is impossible to use the RT-toolbox in our platform, because our system requires real-time communication, online decision-making, and path planning.

We therefore applied robot protocol and send protocol commands to the robot controller through a TCP socket. The advantage of the robot protocol code is that programmers can embed the command in their customized software with other computer languages.

The robot arm controller works as a TCP server and the robot control module works as a TCP client; they are connected by Ethernet cable. In the communication mechanism, the client must open a channel using an "OPEN=TOLL" command, followed by operation enable, turning on servo, movement programming, turning off servo and disconnection. Figure 2.6 shows the robot arm protocol programming structure. The robot controller returns feedback for every client request instruction using: Qok<Answer> or QeR<Error No.>.
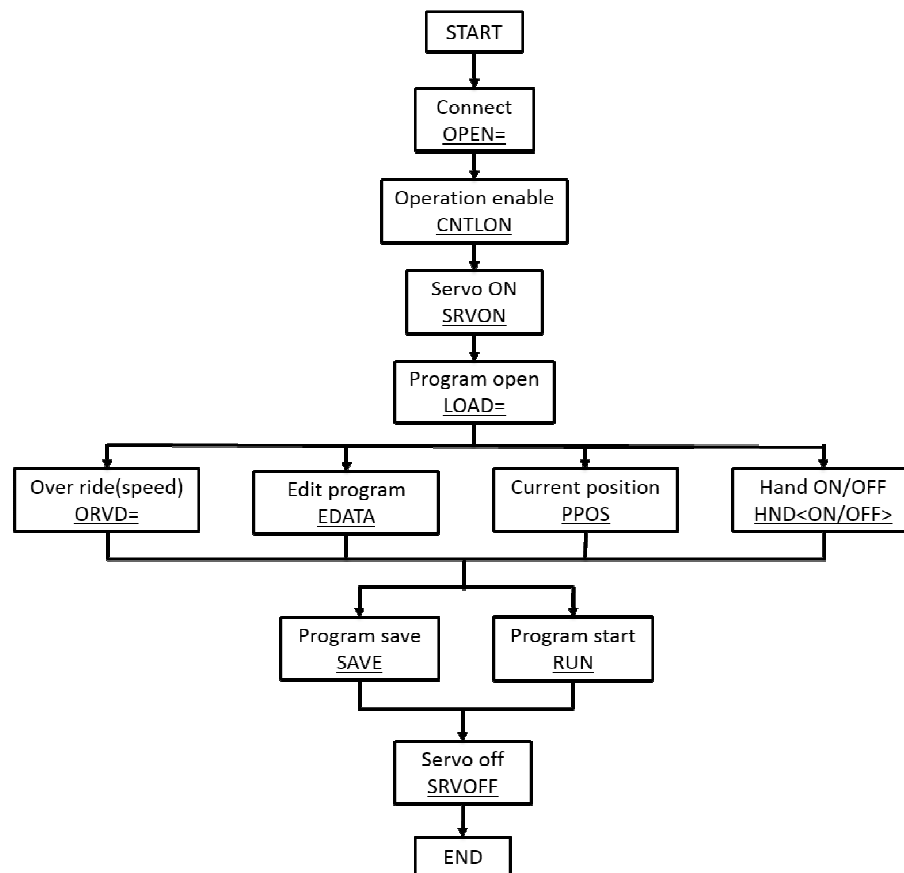
Figure 2.6. *Robot arm programming flow chart.*

2.3.3.3 ToF camera control module and data processing module

The SR_4000 (MESA Imaging AG, Switzerland) is a 3D camera based on a Time-of-Flight principle. The camera works as an active IR-light illumination source, and the object of study reflects the IR light back to the camera sensor. The camera measures the time taken for the light to travel between transmitting and receiving. The data output from SR_4000 is a 176×144 matrix, with each element including x, y, and z values.

The camera control module constantly provides a status signal to the main control module after the system turns on. When these two conditions are satisfied: camera status is set to "succeed" and when the robot arm has arrived at the target positon, the central module generates an event and the camera module triggers the sensor to acquire an image in response to this event. A calibrated output stream will be transmitted to the camera module from the sensor though a USB connection. The data generates a "<positon No>.pcd" file in memory and the camera module will send an event to the main module after completing image acquisition.

When the main module responds to the imaging completion event, the data processing module becomes active; the details of the processing algorithm are discussed in the next chapter. Processing results will be transmitted to the main module for visualization on the user interface.

2.3.4 3D image pre-processing and segmentation

Point cloud pre-processing and leaf-stem segmentation is one component of the data processing module. Pre-processing provides background and noise filtering as well as

multiple-views data merging. In the leaf-stem segmentation algorithm, we first project 3D

data into the 2D z-y plane, then apply the y-axis pixels density distribution method to obtain

stem positions on the y-axis. After isolating the stem point clouds, the remaining points will

be separated into several leaf clusters.

2.3.4.1 Multi-view images

  To reconstruct more details, multi-view images instead of a single front view are

produced. The standard field of view range of the SR_4000 ToF camera is 43° (horizontal) ×

34° (vertical). The maize seedling is placed 550~800 mm in front of the origin of the robot

arm base coordinate; the distance between the center of the sensor and the plant is 800 mm.

The movement of the robot arm is 0~859 mm of independent freedom along the z axis, -

642~642mm of independent freedom along the y axis, and -330~642 mm of independent

freedom along the x axis. In fact, the movement is limited when all 6 joints work together,

and the range is complex and changeable when considering the axis rotations, i.e., yaw, pitch,

and roll, of the end-effector frame. In this project the system acquired the 3D plant data from

3 views of the object. The corn plant is placed in front of the robot arm. Figure 2.7 shows the

right, middle and left views of the plant in robot arm base coordinates.
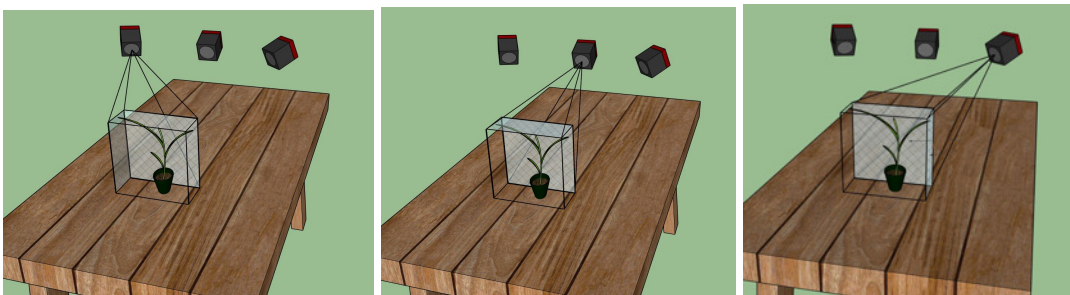
Figure 2.7. 3D data acquisition in multi-views.

  At each viewpoint, the robot arm produces a homogenous transformation matrix to

describe the relationship between the end-effector frame and the robot arm base coordinates.

All data from different viewpoints can be transformed into base coordinates by implementing

Equation 2.3:

$$\begin{bmatrix} x \\ y \\ z \\ 1 \end{bmatrix}_{base} = \begin{bmatrix} x \\ y \\ z \\ 1 \end{bmatrix}_{Camera} *[R\,|\,T]_{cam-to-end} *[R\,|\,T]_{end-to-base} \qquad 2.3$$

The camera to end-effector transformation matrix is calculated by a calibration method, and

the end-effector to base transformation matrix is produced by the robot arm controller.

2.3.4.2 Background and noise removal

The working area is a rectangle 250 mm long by 150 mm wide in front of the origin

of the robot base coordinate along the +x axis direction. The maximum height and width of

the corn seedling are set to be 600 mm and 500 mm. We then only retain the points inside the

range of the cuboid, i.e., within a range of 250 mm (width) × 500 mm (length) × 600 mm

(height) to eliminate the table and wall backgrounds.

It is typical for a ToF to generate point clouds with varying densities; the raw data of

the corn point cloud always contains a few sparsely-distributed outlier points. The statistical

outlier removal algorithm treats a point as outlier or inlier according to the distance to its k-

nearest neighbors (Rusu, et al., 2008). This threshold is set as $\mu + \beta\sigma$, where μ is the average

and the σ is the standard deviation of the k neighbor distances. The k-nearest neighbors

distance value of sparse points is normally greater than the threshold, $\mu + \beta\sigma$.

The value of β represents the key effect of the filtering results. If the β is too small, only a

few noise points are removed; if too high, some points of the plant could be mistakenly

removed. We used k = 10 and β = 10 as filter parameters, as recommended in the literature (Chaivivatrakul et al. 2014).

2.3.4.3 Leaf and stem segmentation

Parameter computation and trait extraction are based on segmentation, because an individual component, such as one leaf, is easier to morphologically analyze. In 3D leaf and stem segmentation, Chaivivatrakul, et al., (2014) sliced the corn point cloud from stem bottom to leaf top, and performed least-squares ellipse fitting for each module. The linked ellipses with close center and semi-major axis length are considered as stem parts. Li (2014) projected the 3D corn point cloud into 6 binary images from 0, 60, 120, 180, 240, and 300 degree view angles. If a straight line has over 50 pixels and inclination angle is between -5° and +5°, this system would treat this line as the stem.

In our segmentation algorithm, the corn point cloud is projected as a binary image. The white pixels belonging to the plant are given value 1 and the black pixels are given value 0 in the image. In this research, the stems of our corn plants normally lie at angles between 85°~95° with respect to ground.
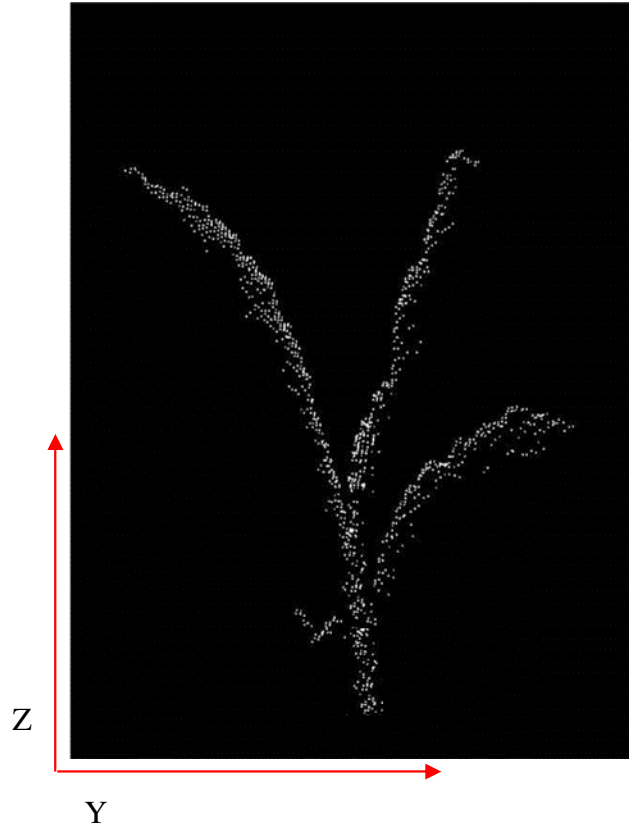
Figure 2.8. *2D projection binary image*

We next calculate how many white pixels there are in each unit in the y direction, generating a pixel density distribution map along the y axis. Because the stem part is approximately vertical, it must have the highest density in the distribution map. The y value of the highest density area is the location of the stem on the y axis (Figure 2.8), so we can obtain the stem by retaining the points in this interval.
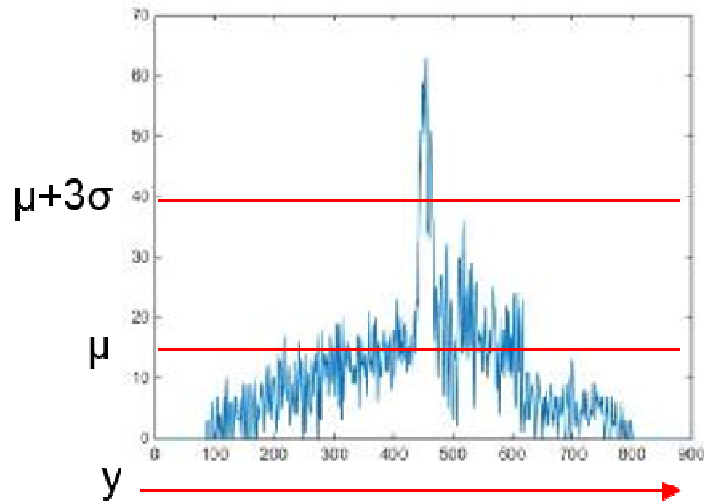
Figure 2.9. *Projected point distribution in y direction*

After extracting the stem point cloud, the remaining points correspond to the leaves. To separate the leaf points into several single ones, a clustering method called "Euclidean Cluster Extraction" (Rusu, 2009) is applied in this algorithm. The algorithm should define how a point belongs to a particular point cluster and why it is different from other point clusters. Let p_i, $p_j \in \mathcal{P}$; if the minimum distance from a set of points p_i to p_j is larger than the threshold d_{th}, p_j must belong to another cluster, where the minimum $\| p_i - p_j \| \geq d_{th}$

We create a kd-tree T to represent the input leaves point cloud $\mathcal{P}$ and build a list of clusters L to store the output. If for a point $p_i \in \mathcal{P}$, we add it to a queue Q and search for the set p_k that is the neighbors of p_i in a sphere with radius less than d_{th}. When that step is completed, add the Q to the leaf cluster L_k. After traversing all p_i, the segmented leaf clusters are stored in L.
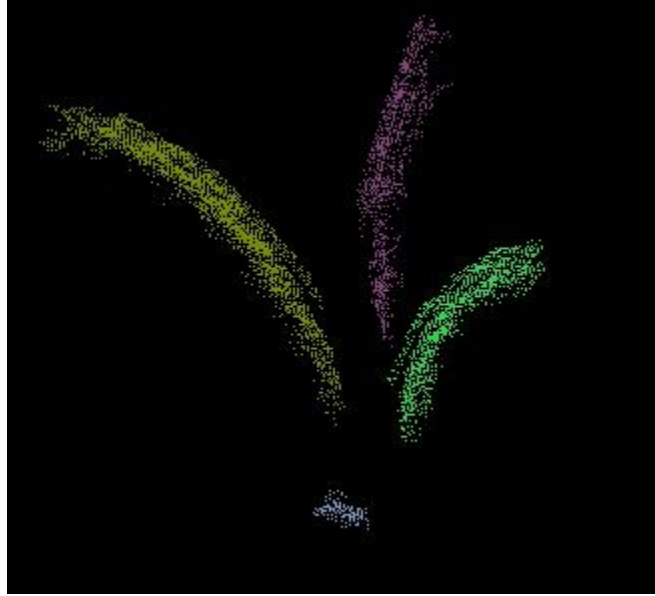
Figure 2.10. *Separated leaf clusters*

2.3.4.4 Leaf curve fitting and parameter computation

Before leaf parameter extraction, the algorithm uses a high-order 3D curve to describe the skeleton of each leaf. In the x-y plane, the skeleton of the leaf is a line, and if the leaf is viewed in y-z plane, the leaf skeleton is a curve. We can thus split the high-order 3D curve into 2 equations:

$$x = k \times y + b \tag{2.4}$$

$$z = \beta_0 + \beta_1 \times y + \beta_2 \times y^2 + \ldots + \beta_k \times y^k \tag{2.5}$$
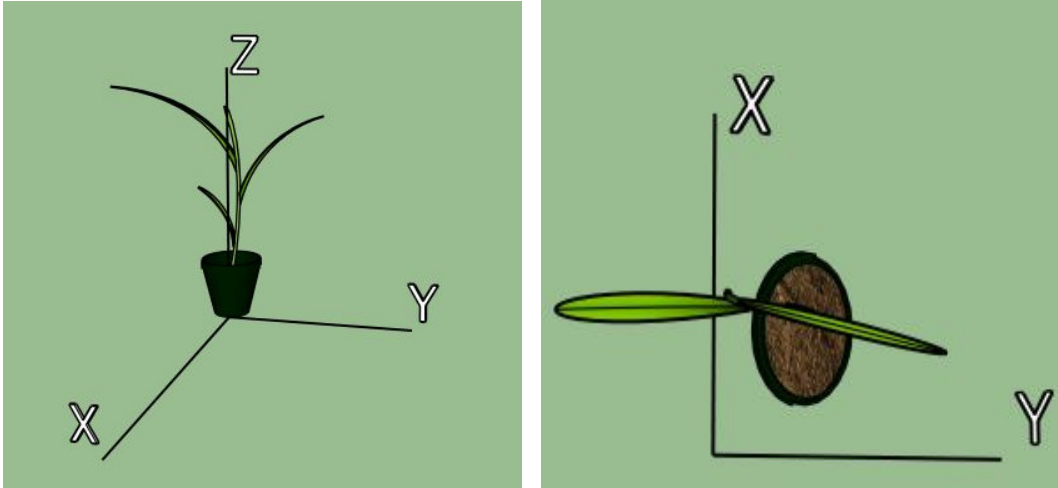
Figure 2.11. *Right is the plant in y-z plane, left is the plant in x-y plane.*

In the y-z plane, the leaf skeleton with greater curvature must have a larger k value. There are 97 leaves, ranging in length from 50 mm to 521 mm, chosen randomly to test which order is suitable in this project. When compared with the ground-truth, the error distribution plot and a summary statistics table are given by:

$$Error = \frac{\| system\ output - groundtruth \|}{groundtruth} \times 100\% \qquad\qquad 2.6$$

The "second order" mean of error is 0.1316, and is the smaller than that of first order (0.1525) and third order (0.1559). The "second order" mean of error is the smallest. Thus we set k equal to 3, a condition that is satisfied under most situations.
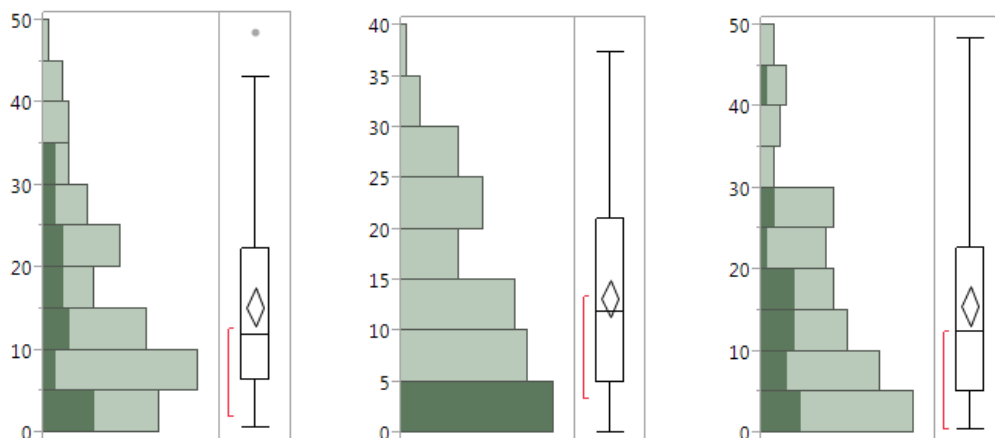
Figure 2.12. Leaf length error distribution with different order value. (Left is 2 order, middle is 3 order, left is 4 order)

Table 2.1. Leaf length error estimated by different orders fitting (%)

Quantiles								
k = 2 (second order)			k = 3 (third order)			k = 4 (forth order)		
100%	maximum	48.3818	100%	maximum	37.3484	100%	maximum	48.3727
75%	quartile	22.3707	75%	quartile	21.0474	75%	quartile	22.7412
50%	median	11.8846	50%	median	11.8308	50%	median	12.3604
25%	quartile	6.4128	25%	quartile	4.9859	25%	quartile	5.0897
0%	minimum	0.5967	0 %	minimum	0.0232	0 %	minimum	0.4439

Summary Statistics					
Mean	15.2481	Mean	13.1608	Mean	15.5949
Std Dev	11.4582	Std Dev	9.0656	Std Dev	12.0881
Std Err Mean	1.1634	Std Err Mean	0.9204	Std Err Mean	1.2273
Upper 95% Mean	17.5574	Upper 95% Mean	14.9880	Upper 95% Mean	18.0313
Lower 95% Mean	12.9387	Lower 95% Mean	11.3337	Lower 95% Mean	13.1586
N	97	N	97	N	97

The y range of the leaf is divided into N subsections. For each y value, there are corresponding x and z values to make up a leaf point (x, y, z). When these points are connected, the curve created is the leaf skeleton.
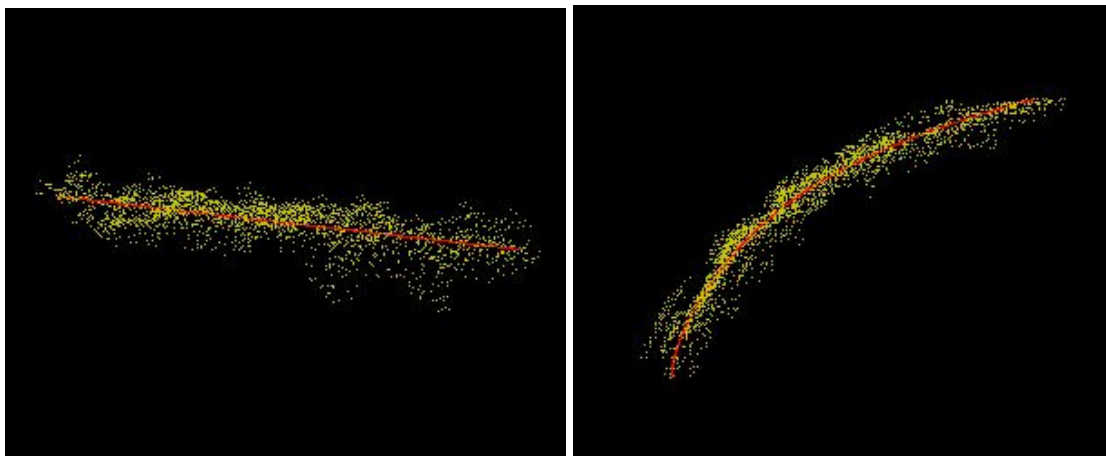
Figure 2.13. Right red line is the leaf fitting in y-z plane, left red line is the plant in x-y plane.

Based on the leaf skeleton fitting curve, the length of the leaf is the sum of N fractional lengths.

$$Length = \sum_{i=1}^{N} \sqrt{(x_i - x_{i-1})^2 + (y_i - y_{i-1})^2 + (z_i - z_{i-1})^2} \qquad 2.7$$

For stem model estimation, we fit it as a cylinder and compensate the bottom part through lost filtering. The length of the stem is the highest z value minus the distance between the desktop and the bottom of the stem.
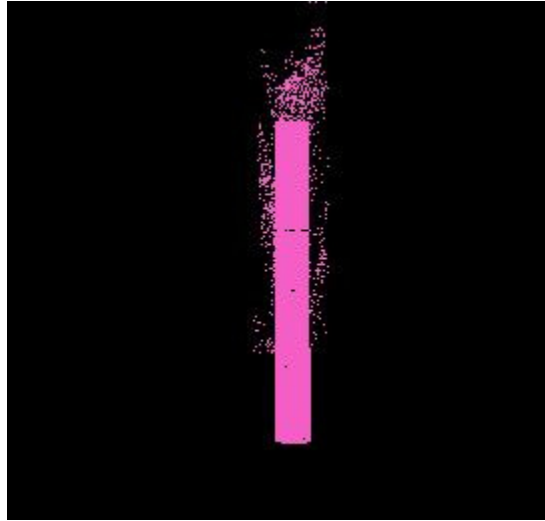
Figure 2.14. Stem fitting model.

2.4 Results and Discussion

In this section, the detailed experimental setup and operational steps are discussed. We describe functional flow to illuminate how the human/machine interface works, a 3D image-acquisition procedure, and data processing with final result visualization. The experimental objects were 60 maize plants at V2 ~ V5 stages. We provide the result of each phenotype for all leaves and plants, analyze the system measurement error related to ground truth, and finally draw conclusions.

2.4.1 Results and error analysis

After placing the plant on the working area of the desk, we power up the robot arm

controller and check the hardware connection. We then start up the software and check

communication between the interface and the ToF camera. When the status of the camera is

indicated as "succeed", we begin system operation.

The first step is to press the "Acquire 3D data" button. The robot arm will bring the ToF

camera to different positions to begin collection of the 3D point cloud plant data. When the

"process 3D data" button is pressed as shown in Figure 2.15, the software will process the

data collected. After the process bar indicates 100%, the reconstructed corn plant model will

be displayed, and the user can then rotate and zoom in/out on this display as desired. The

stem and different leaves will be labeled with different colors. At the same time, a table will

display the parameters of the plant, e.g., the lengths of each leaf and the stem height.
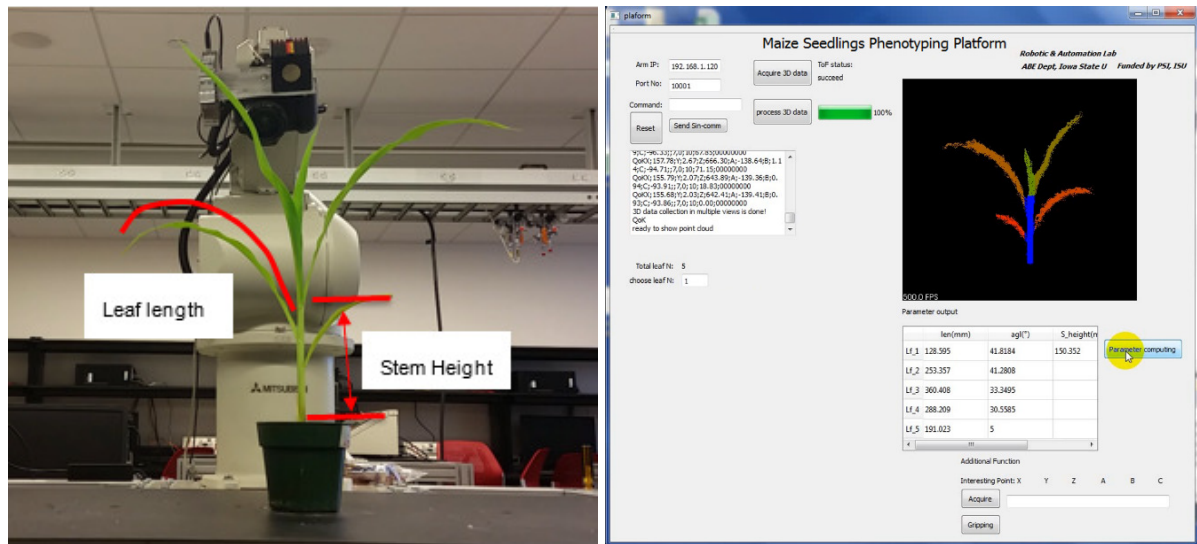
Figure 2.15. *Working area (left) and Parameter output in the user interface (right).*

We grew 60 maize plants in the growth chamber, and we began to collect data 7 days

after they sprouted. Every 3 days we measured the plants using the system and they were also

measured by hand; the measured parameters included stem height and leaf length. The results

measured by hand were treated as ground-truth. We took 9 measurements from the plants on

days 8, 11, 14, 17, 20, 23, 26, 29, and 32. 534 stem heights were measured (2 plants were

dead on day 29, and 2 plants were dead in day 32), and a total of 1969 leaves were tested

during this experiment.
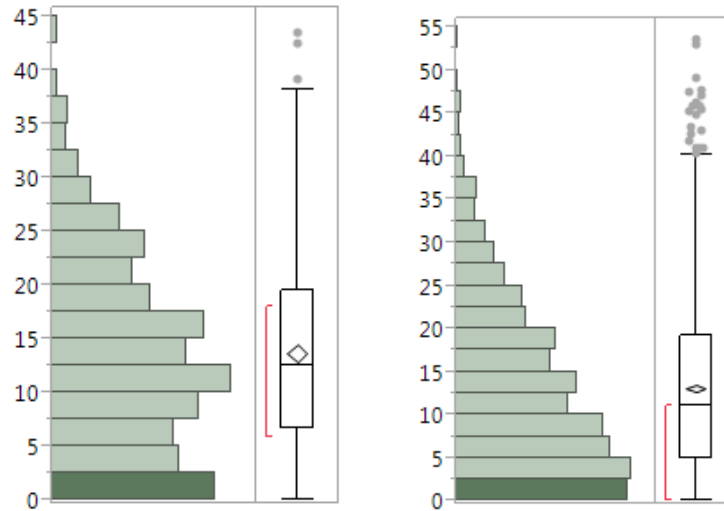
Figure 2.16. *Error (%) distribution of the stem height (right) and leaf length (left) system measurement*

Figure 2.16 is the error distribution of stem height and leaf length. These are half-

normal distributions and their mean and median values are closed. There is no obvious bias

shown in the error distributions, meaning that the measurements did not overestimate or

underestimate the true values.

Table 2.2. *Stem height Error table (%)*

Quantiles			Summary Statistics	
100%	maximum	43.5500	Mean	13.6721
75%	quartile	19.4917	Std Dev	8.9439
50%	median	12.5129	Std Err Mean	0.3870
25. %	quartile	6.6000	Upper 95% Mean	14.4325
0%	minimum	0.0166	Lower 95% Mean	12.9119
			N	534

Table 2.3. *Leaf length Error table (%)*

Quantiles			Summary Statistics	
100%	maximum	53.5031	Mean	13.0979
75 %	quartile	19.1725	Std Dev	9.8813
50%	median	11.0794	Std Err Mean	0.2227
25%	quartile	5.0017	Upper 95% Mean	13.5345
0 %	minimum	0	Lower 95% Mean	12.6611
			N	1969

The stem heights of these corn plants ranged from 30 mm to 220 mm, the length of the leaves ranged from 20 mm to 567 mm; a total of 534 stems and 1969 leaves were measured. Table 2.2 shows that the error of stem height is 12.5129 % (median value) and 13.6721 % (mean value). The minimum error between the measurements and ground-truth were approximately 0%. More than 75 % of stem height measurements exhibited error less than 20%. A quarter of the stem height measurements have very small errors (6.6%). The confidence interval (95 %) of the error mean is 12.91 % ~ 14.43%. The leaf length measurement error is 11.0794 %(median value) and 13.0979 %(mean value). A quarter of the measurements of leaf length have an error of 5 %, and three quarters of the measurements have an error rate less than 20 %. However, there are outliers with values over 40% in the error distribution. Such large errors usually happened when the stems were as low as 30 ~ 60 mm. The ToF sensor contributes a 10 mm error, close to the stem height, so a large relative error value may occur if stems are low. The error comes from the ToF camera (10 mm), filtering and leaf curve fitting. The choice of filter parameters and the order of fitting curve to satisfy all situations is difficult because each plant has differently shaped leaves. The surface of a corn leaf is not flat, and the fluctuating part of the leaf may have high density. Some leaves are more bent than others, so more than 3-order is required to adequately present the skeleton.

2.4.2 Discussion and Conclusion

In this project, the results of phenotype extraction for maize seedlings have demonstrated the feasibility of this automatic phenotyping system. Three sources make contributions to the error: filters, ToF accuracy, and the curve-fitting algorithm. The ToF camera we used in this project has a resolution of only 176×144, so to improve the accuracy of the system, a higher resolution 3D sensor is needed. The filter parameters are also very important to the conduct of system measurement. We used pass-through and outlier remover filters in this project and, because these two filters are sensitive to plant shape, it is difficult to choose fixed values for filter parameters to satisfy all situations. If color data can be used to remove the noise the measurement error would decrease. A RGB threshold can be used to retain green parts (corn plants) and remove background and noise. This threshold could be applied for different shaped plants because the color of the corn plants varies very little. The current system considers only the shape of the plant but, in addition to measuring plant morphology character, there are several other phenotyping traits we care about. Different sensors, such as those in a color camera, are required to observe texture changes of the leaf.

In future work, we will execute probing of the plant based using a 3D model of the seedlings. The Kinect V2 (Microsoft, USA) is an ideal sensor we may consider; it combines a high resolution ToF camera (512×424) and color camera (1920×1080). The 3D data and color data can be transferred into the same coordinate system using built-in functions of its SDK. Such a system would be able to acquire both morphology characters and color traits of the corn plants at the same time. We should test the system on a wider range of corn plant growth stages and try to follow the growth of seedlings.

REFERENCES

Dornbusch, T., Wernecke, P., Diepenbrock, W., 2007. A method to extract morphological traits of plant organs from 3D point clouds as a database for an architectural plant model. Ecological Modeling 200, pp. 119-129.

De Moraes Frasson, R.P., Krajewski, W.F., 2010. Three-dimensional digital model of a maize plant. Agricultural and Forest Meteorology 150, pp. 478-488.

Ijiri, T., Owada, S., Okabe, M., Igarashi, T., 2005. Floral diagrams and inflorescences: interactive flower modeling using botanical structural constraints, in: ACM Transaction on Graphics (TOC), ACM, and New York, NY, USA. pp. 720-726.

Ulrich Weiss, Peter Biber, Plant detection and mapping for agricultural robots using a 3D LIDAR sensor, Robotics and Autonomous Systems, Volume 59, Issue 5, May 2011, pp. 265-273.

Watanabe, T., Hanan, J.S., Room, Peter M.and Hasegawa, T., Nakagawa, H., Takahashi, W., 2005. Rice morphogenesis and plant architecture: Measurement, specification and the reconstruction of structural development by 3d architectural modeling. Annals of Botany, pp. 1131-1143.

Yann Chéné, David Rousseau, Philippe Lucidarme, Jessica Bertheloot, Valérie Caffier, Philippe Morel, Étienne Belin, François Chapeau-Blondeau, On the use of depth camera for 3D phenotyping of entire plants, Computers and Electronics in Agriculture, Volume 82, March 2012, pp. 122-12.

G. Aleny`a, B. Dellen and C. Torras, 3D modelling of leaves from color and ToF data for robotized plant measuring, 2011 IEEE International Conference on Robotics and Automation [1050-4729] Alenya, G yr:2011 pg:3408 -3414.

G. Feng, C. Qizin, and M. Masateru, "Fruit detachment and classification method for strawberry harvesting robot", International Journal of Advanced Robotic Systems, vol 5, pp. 41-48, 2008.

Ch.-H. Teng, Y.-T. Kuo, and Y.-S. Chen, "Leaf segmentation, classification, and three-dimensional recovery from a few images with close viewpoints". Optical Engineering 50(3), doi:10.1117/1.3549927, 2011.

R. Klose, J. Penlington and A. Ruckelshausen: "Usability study of 3D Time-of-Flight cameras for automatic plant phenotyping", Workshop on Computer Image Analysis in Agriculture, pp. 93-105, August 2009.

Foundation, N. S., and G. Mcb. Phenomics: Genotype to Phenotype A report of the Phenomics workshop sponsored by the USDA and NSF, 2011.

Kahn, Svenja; Haumann, Dominik; Willert, Volke. "Hand-eye calibration with a depth camera: 2D or 3D", International Conference on Computer Vision Theory and Applications (VISAPP), pp.481-489, 2014.

Rusu, R.B., Cousins, S., 2011. 3D is here: Point Cloud Library (PCL), in: IEEE International Conference on Robotics and Automation (ICRA), Shanghai, China. pp. 1-4.

Supawadee Chaivivatrakul, Lie Tang, Matthew N. Dailey, Akash D. Nakarmi, Automatic morphological trait characterization for corn plants via 3D holographic reconstruction, Computers and Electronics in Agriculture, Volume 109, November 2014, Pages 109-123, ISSN 0168-1699.

Ji Li. (2014). 3D machine vision system for robotic weeding and plant phenotyping. PhD dissertation, Iowa State University, USA.

Radu Bogdan Rusu. (2009). Semantic 3D Object Maps for Everyday Manipulation in Human Living Environments. PhD dissertation, Technischen Universität München, Germany.

Christian Wengert, Mireille Reeff, Philippe C. Cattin, Gábor Székely. "Fully Automatic Endoscope Calibration for Intraoperative Use" Bildverarbeitung für die Medizin Informatik aktuell 2006, pp 419-423.

CHAPTER 3. DEVELOPMENT OF AN AUTOMATED MAIZE FUNCTIONAL GENOMICS PLATFROM

3.1 Abstract

Characterizing genes and their functions is an important step required for the discovery and introduction of genetic traits beneficial to crop plants and increased production. One approach to gene discovery involves the use of viral vectors that can be used to overexpress genes or for virus-induced gene silencing to reduce gene expression, creating gain-of-function and loss-of-function phenotypes, respectively. Successful use of viral vectors in corn plants will create a need to rapidly and efficiently associate many genes with phenotypes or traits. This research project combined sensors with custom algorithms to implement a system that can distinguish virus-infected plants from non-infected plants, the first critical step in construction of an automated phenotyping platform. An industrial robot arm positions a Time-of-Flight (ToF) camera to different viewing points to obtain 3D depth data from each corn plant. After 3D reconstruction and leaf and stem segmentation, the robot arm brings a color camera to the target position to obtain the leaf's color image. This automated maize gene function discovery platform can discern virus-infected and non-infected maize plants and track their growth as well. The resulting data sets will be used to determine if phenotypes induced by overexpression or silencing genes deviate from those of control plants.

Keywords: Phenotyping, virus-infected plant, genes traits, 3D reconstruction, robot arm, ToF camera

3.2 Introduction

Crop breeding plays an important role in modern agriculture by improving plant adaptation and increasing yields. Phenotype parameters, including leaf and stem size, plant height, nutrient intake rate, cereal yield, and disease resistance, are crucial for breeders (Foundation and Mcb, 2011). Understanding the relationships between genotypes and crop traits is the key to optimization of breeding, but the requirements of mass data collection and analysis make manually phenotyping difficult and tedious.

Benefitting from modern imaging techniques improvement, multi-parameter data and multi-dimensional visualization have been achieved. No matter the kind of crop environment, e.g., growth chambers, greenhouses, or fields, image techniques are capable of quantifying complex traits (Arvidsson, et al., 2011). Current imaging techniques used in plant phenotyping include visible imaging, fluorescence imaging, near-infrared imaging, 3D imaging, laser imaging, and x-ray tomography (Lei, et al., 2014).

One popular imaging technique is 3D plant mapping; presently available imaging sensors include laser scanners, stereo vision, time-of-flight cameras, and even consumer-gaming interfaces like Microsoft Kinect (Azzari, et al., 2013). Stereo vision normally requires two or more sensors to produce 3D data, and the reconstruction result and depth accuracy are dependent on the type of algorithm. Moreover, the surface texture of the object can affect the performance of the stereo algorithm. Jin, et al. (2009) have implemented stereo imaging in corn plant 3D reconstruction. Their algorithm is able to detect each corn plant and find its center in the field using depth information.

Among stereo imaging techniques, a time-of-fight camera can produce a 3D point cloud directly and more quickly. Current ToF camera technique involves obtaining 50 frames

per second. Alenya, et al., (2011) mounted a ToF camera on an industrial robot arm for indoor plant phenotyping. They combined depth data and RGB images for leaf segmentation. After determining the position of the leaf, they drive the robot arm closer to the leaf to obtain leaf-surface details. Their work proves that the depth map provided by a ToF camera combined with a color image can yield good point cloud data for plant parameter measurements.

A ToF camera has also been used for counting corn plants in the field (Nakarmi, et al., 2012). Their system combined depth information with an intensity map to measure the spacing between plants in a crop row. This system solved the problem of applying a ToF camera under outdoor conditions by using an umbrella to cast a shadow over the imaging area. Song, et al., (2011) combined a stereo camera with a ToF camera to estimate a dense depth map for automatic plant phenotyping. The ToF image data enhances the performance of the stereo camera and their system was able to reconstruct a 3D colored leaf under greenhouse conditions.

Visible imaging techniques have been widely applied in plant science because of their low cost and ease of operation (Lei, et al., 2014). Shitala, et al,. (2011) developed an automated system to detect the crop diseases based on leaf color image. Their system can isolate the diseased region of a leaf by analyzing image energy. Zulkifli, et al., (2013) built an imaging processing platform to deal with Chili leaf disease detection issues. They used RGB threshold, complementation, edging, and color comparison in diseased region image recognition.

However, up to now there has been no system combining robotic techniques with 3D and color imaging for plant phenotyping and infected leaf detection. In this paper, we

describe developing an automatic phenotyping platform capable of characterizing maize plant traits, detecting infected plants, and probing the leaves.

3.3 Materials and Method

An overview of the system is shown in Figure 3.1. It is composed of a time-of-flight (ToF) camera (SR_4000, MESA Imaging, Switzerland), an industrial robot am (RV_3SD, Mitsubishi, Japan), a color camera (EOS 6D, Canon, Japan), a robot hand (Robohand, Destaco, USA), and a computer station. In the HMI (Human-machine interaction) interface, the user presses "Acquire 3D data" and "process data" buttons to acquire 3D images through the ToF camera. After image processing, the segmented leaves and stem are visualized in the window. Depending on user requirements, the robot arm may grasp the selected leaf. The robot arm will also be able to approach the leaf center and take a picture using the Canon 6D still camera. The system will perform conversion of RGB to HSV, color segmentation, leaf region extraction, perform a Gray-level Co-occurrence Matrix (GLCM) parameter analysis, and implement Bayes classification. Eventually, the diagnostic result (infected or not) will be displayed by the interface.
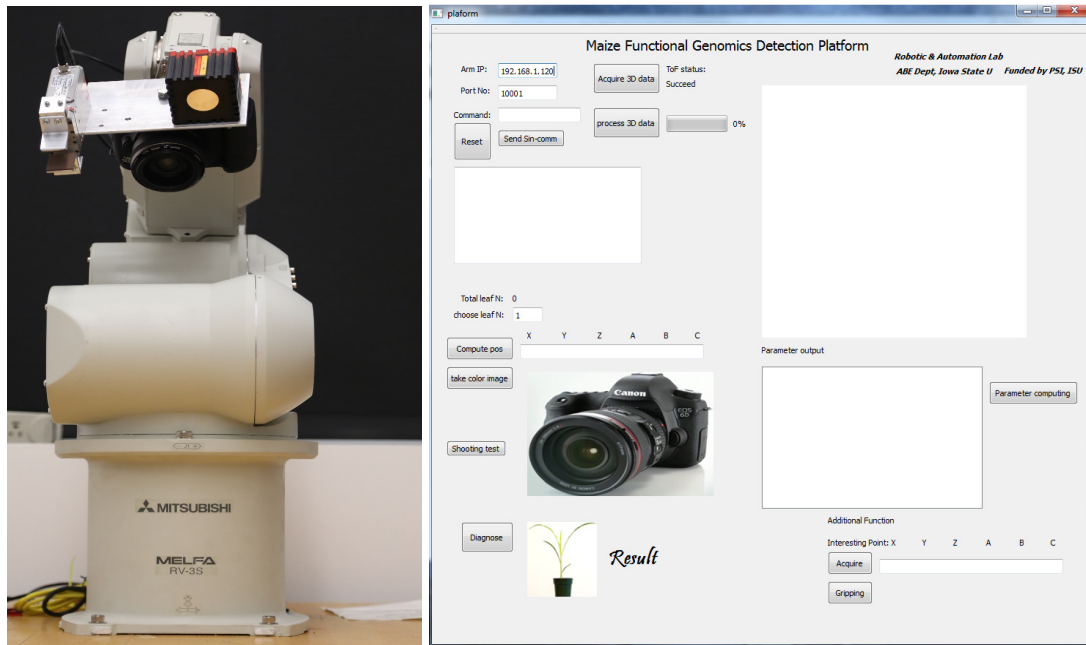
Figure 3.1. Hardware and user interface overview

3.3.1 3D image acquiring and processing

After placing the maize plant on the working area, the system will take 3D pictures of the plant in multi-views with the ToF camera. The platform applies pass-through filtering and statistical outlier removal algorithms to remove the background and noise points. We implement a 3D-to-2D projection method and a pixel density distribution map to segment the stem and leaves. A 3D curve-fitting algorithm is used to produce plant phenotypic parameters. Each leaf point cloud is labeled with a different color in the visualization window. System details are discussed in Chapter 2.
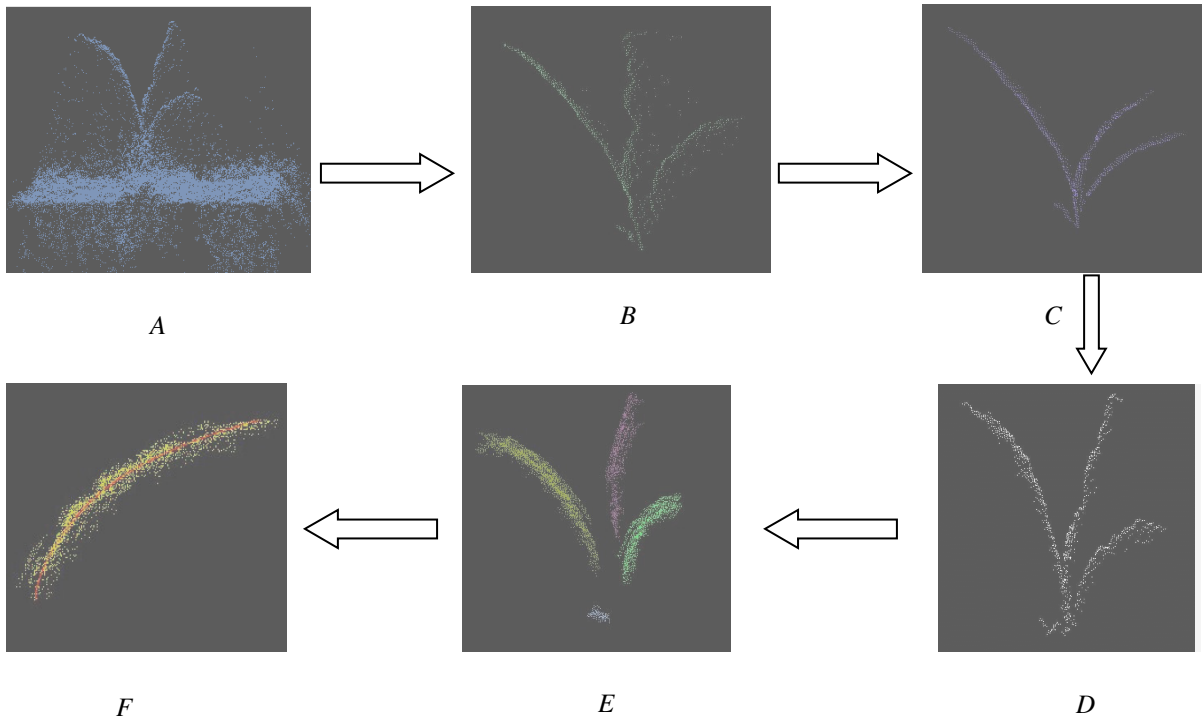
Figure 3.2. *Maize 3D model reconstruction. A is the original data in robot base coordinate. B &C is clean plant point cloud after filtering. D is 2D projection map. E is the segmented leaves clusters. F is the leaf skeleton fitting.*

3.3.2 Canon 6D hand-eye calibration

The leaf positon is taken to be the robot base coordinate. To estimate the 3D position and orientation of the target object related to the Canon camera coordinate frame, it is essential to know the relationship between the camera and the robot end-effector. In addition to the low-resolution images from the ToF camera, the Canon 6D can provide high quality color images. It is thus feasible to apply a fully vision-based calibration method to calculate their transformation matrix, and we used the Hand-Eye calibration Toolbox (Christian W, 2006) for this purpose.
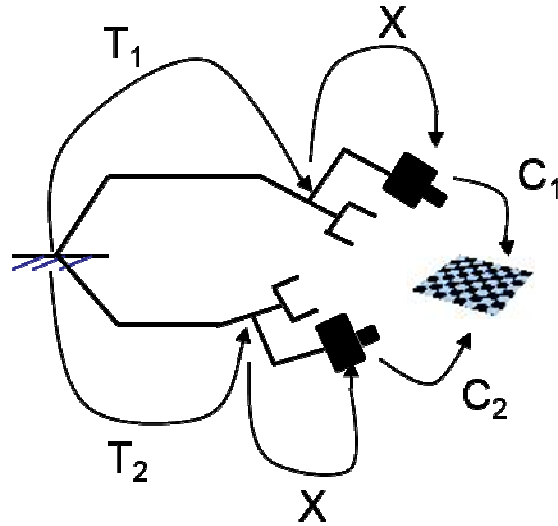
Figure 3.3. *Hand-eye calibration.*

The robot arm moves the Canon 6D to 10 different positions for chessboard pictures, and we record each homogeneous transformation matrix between the robot arm end-effector and the base coordinate frame. This toolbox will solve 10 sets of homogeneous transform equations of type AX=XB, where X is the target homogenous transformation matrix.
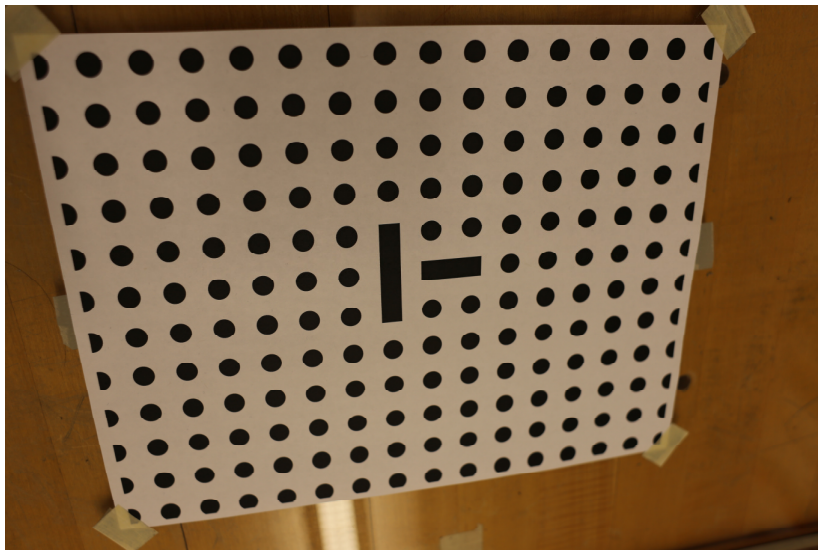
Figure 3.4. *Chessboard image*

$$R_{Canon} = \begin{bmatrix} -0.9959, -0.0867, -0.0255 \\ 0.0858, -0.9957, 0.0348 \\ -0.0284, 0.0324, 0.9991 \end{bmatrix} \qquad 3.1$$

$$T_{Canon} = \begin{bmatrix} 13.8124 \\ 4.7601 \\ 112.9481 \end{bmatrix}, \text{ where the unit is mm.} \qquad 3.2$$

Each Canon 6D camera has its own individual optical center even though they are manufactured in the same batch. If we assume the center of the lens body to be the optical center, the transformation matrix between the camera's coordinate system and the end-effector frame can be estimated. With respect to the dimension of the mounting bracket, the matrix is described as follows.

Figure 3.5. *Canon camera coordinate*

$$R'_{Canon} = \begin{bmatrix} -1, 0, 0 \\ 0, -1, 0 \\ 0, 0, 1 \end{bmatrix} \qquad 3.3$$

$$T'_{Canon} = \begin{bmatrix} 5.2130 \\ 11.1290 \\ 106.0250 \end{bmatrix}, \text{ where the unit is mm.} \qquad 3.4$$

The transformation matrix estimation obtained from the dimension method matches the result from a vision-based calibration method.

3.3.3 Leaf skeleton fitting and probing

In Chapter 2, the leaf skeleton was described as a high-order 3D curve, with the leaf length estimated as the sum of N curve fractions. It is easy to locate the middle point of the fitting curve using the length equation. We obtain a triangle by connecting the first point, the final point, and the middle point of the curve. This triangle and the fitting curve are in the same plane, called the triangle plane.
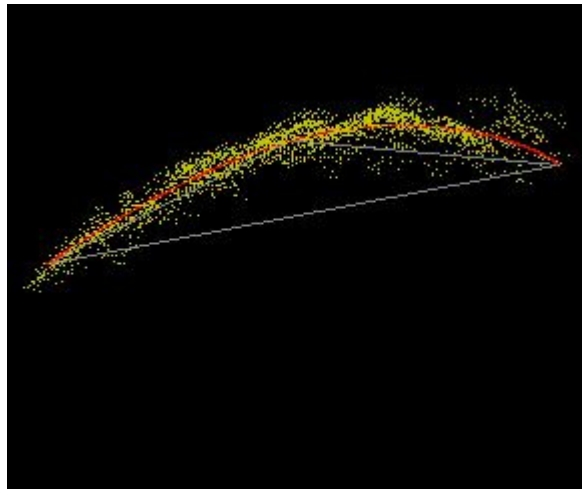
Figure 3.6. Leaf skeleton fitting

We make the middle point the probing target, and require the robot hand finger to be positioned towards the outer normal vector of the triangle plane. The triangle plant normal vector is produced by the cross product of two edges of the triangle. In addition to this triangle normal vector, we also require the normal vector of the leaf surface at the middle point. The leaf surface is curved, so each point has a different normal direction. There are many different methods to estimate the surface normal vector; we applied one of the simplest algorithms. The normal vector of a point on the surface is can be approximated by the normal

of a plane tangent to the surface to that point. We can then solve the normal vector estimation problem by least-squares plane fitting (Rusu, 2009). In this project, we call a function, "Normal-Estimation (PCL)", to obtain the normal of the middle point on the leaf surface.
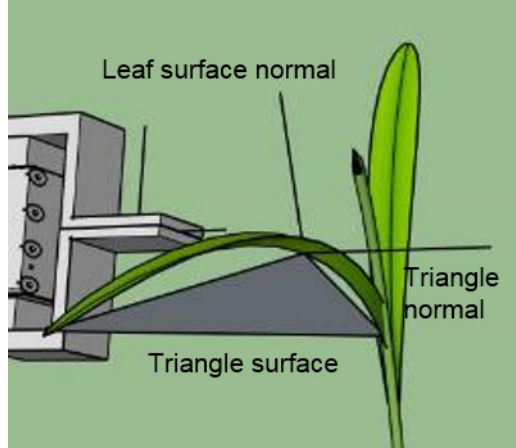
Figure 3.7. *Leaf normal vector and gripper center frame*

Two vectors are known: the normal vector of the triangle plane and the normal vector of the middle point of the leaf surface. A third vector can be produced by the cross product of these two known normal vectors. We can obtain the homogeneous transformation matrix between the leaf middle point frame and the robot arm base coordinates. We then define the center point of the gripper finger as the grasping point, and take the y direction of the gripper towards the surface to be the normal vector of the leaf. The z direction of the gripper is fixed towards the triangle normal vector. The relationships between the base coordinate, the end-effector coordinate, the gripper center coordinate, and the leaf center coordinate are described by the following equations.

$$C_{gripper} = C_{leaf} \hspace{4cm} 3.5$$

$$H_{gripper2end} \times H_{end2base} = H_{leaf2base} \hspace{2cm} 3.6$$

—

The transformation matrix between the gripper and the end-effector can be found using dimension method, because the sizes of the Robohand Gripper can be obtained from its data sheet; the end-effector position command is produced by Equation 3.7.

$$H_{end\,2\,base} = H_{gripper\,2\,end}^{-1} \times H_{leaf\,2\,base} \qquad\qquad 3.7$$
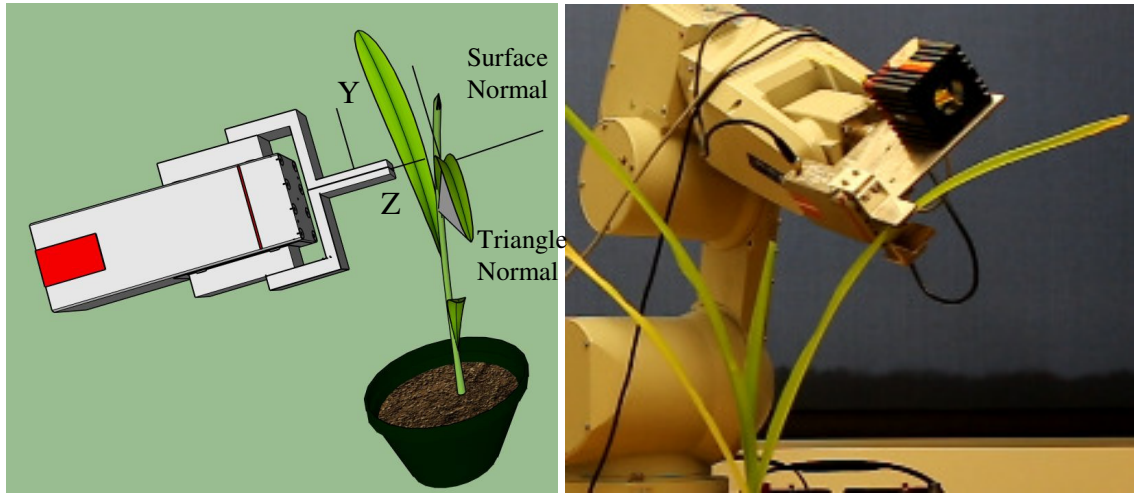
Figure 3.8. *Leaf probing*

3.3.4 Leaf color segmentation and GCLM values extraction

Similarly to the probing process, the leaf center must first be located. The relationship between the leaf center and camera coordinate is known from the hand-eye calibration results for the Canon 6D and the robot arm effector. We make the z direction of the camera against the leaf surface normal, and the x direction of the camera towards the triangle normal. The camera focus distance is fixed at 200 mm to keep the distance between the leaf center and camera optical center constant.
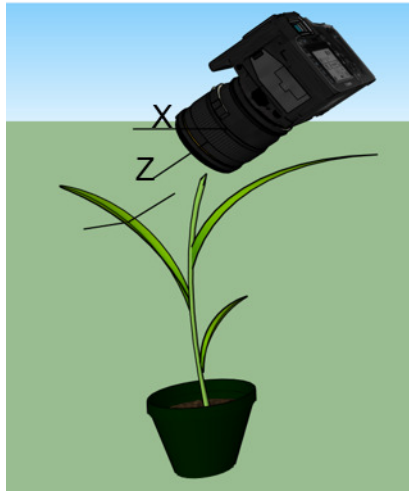
Figure 3.9. *Leaf normal vector and camera frame*

The leaf image produced by system is shown below in Figure 3.10. The center of the image is the intersection of two red lines coinciding with the leaf center. The other reason for fixing the focus length is that this produces the clearest leaf surface and a blurry background.
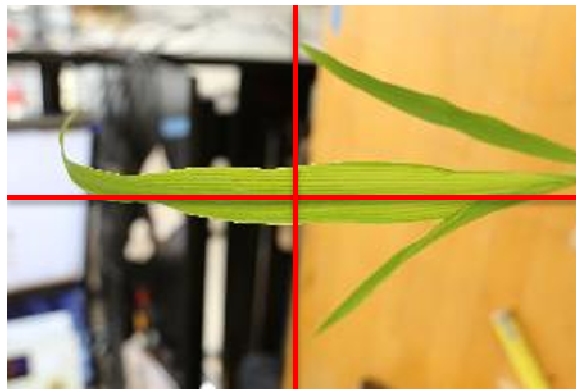
Figure 3.10. *Color image acquisition*

The virus vector is Sugarcane Mosaic Virus (SCMV), and its symptom in infected corn plants is a mosaic color pattern on the leaf surface. While an infected sugar cane leaf texture changes drastically in the field, the symptom of infected corn leaf is not as obvious, so high resolution leaf images and a variety of viewing angles are needed.

To analyze the leaf texture, we take a square window of the leaf color image and transform it into a gray image.

Figure 3.11. *Control leaf color image and texture gray image*
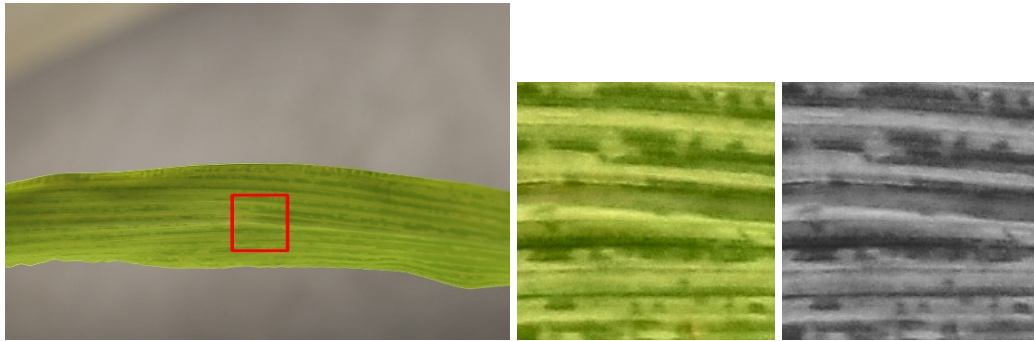
Figure 3.12. *Infected leaf color image and texture gray image*

A Gray-Level Co-Occurrence Matrix (GLCM) is a statistical tool for describing texture characters by considering spatial relationships of pixels in a gray image. We create the GLCM by calculating the frequency of pairs of pixels with specific values occurring in such a gray image and we can then determine statistical parameters from the matrix (Haralick, et al., 1973).
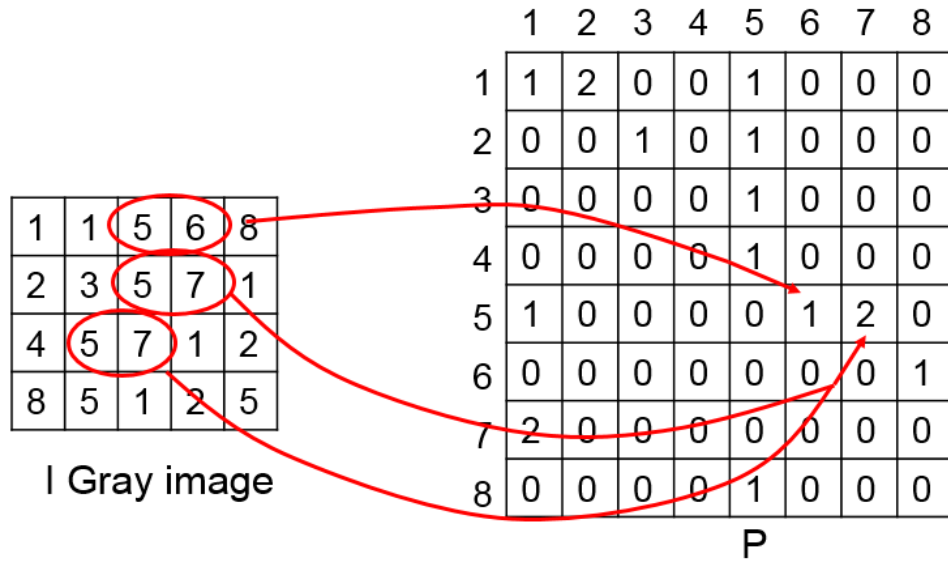
Figure 3.13. *Gray-Level Co-Occurrence Matrix definition*

Fourteen textural features have been proposed for the GLCM (Haralick, et al., 1973). They include homogeneity, energy, entropy, contrast, variance, correlation, sum average, and maximum correlation coefficient.

The energy is also sometimes called Uniformity or Angular Second moment. It describes the textural uniformity, ranging from 0 to 1. If the gray level distributes in a periodic or constant form, the energy value is high.

$$Energy = \sum_i \sum_j P_{i,j}^2 \qquad\qquad 3.8$$

The Homogeneity is also sometimes called a Inverse Difference Moment. It is sensitive to the diagonal elements in the GLCM. When the gray levels of the image are relatively the same, homogeneity has its highest value.

$$Homogeneity = \sum_i \sum_j \frac{1}{1+(i-j)^2} P_{i,j} \qquad\qquad 3.9$$

In this project, the sugarcane mosaic virus infection creates a discontinuous leaf texture. The energy and homogeneity parameters present the periodicity and homogeneity of

the gray image, so the energy and homogeneity values of the control leaf image are higher than that of the infected leaf image. The values of the energy and homogeneity are normalized and shown below in Figure 3.14.
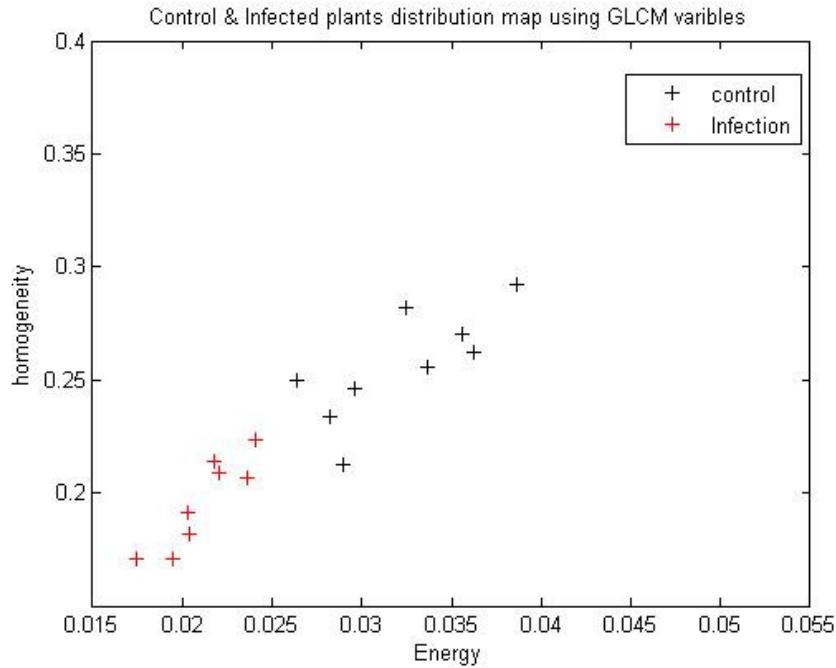
Figure 3.14. Infected and control distribution map

3.3.5 Classification

The purpose of classification is to predict the class of a new unknown sample point based on the former database that has been separated into different classes. Different classification algorithms are implemented depending on the complexity of the database distribution; these include the k-nearest neighbor classifier (KNN), the Bayes classifier and the neural network (NN) classifier. In this research, the distribution of these two classes is separated from the above figure, so we start with a simple classifier, the Naïve Bayes classifier, to try to distinguish infected plants from non-infected plants.

KNN is a non-parametric method used in classification; its output is a class membership. A new sample point is classified by vote of its k nearest neighbors. When k = 1, then this new sample point belongs to its single nearest neighbor. When k = 3 as shown in Figure 3.15, then we find its 3 nearest neighbors. There are two red points and only 1 blue point, so the new sample point is assigned red.
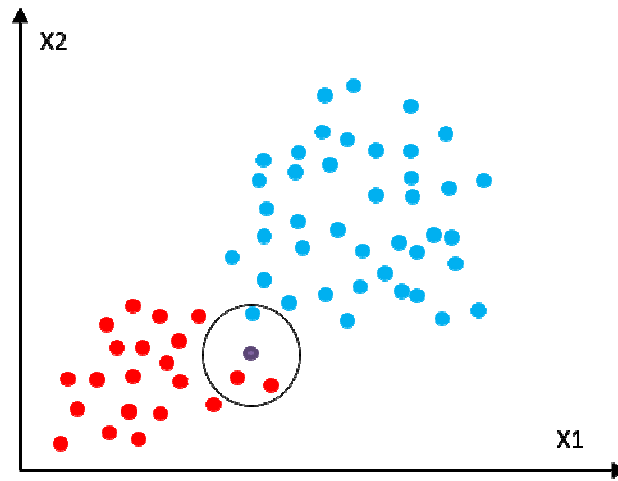
Figure 3.15. Naïve Bayes classification

The Naïve Bayes classifier is a simple probabilistic classifier based on Bayes' theorem. We assume there are d classes and determine which class to which the new sample point belongs. We then calculate the probability of the new sample point as class k, where k ranges from 1 to d based on Bayesian probability, as shown in Equation 3.10.

$$P\{Y = k \mid X_1,...,X_d\} = \frac{P\{Y = k\}f(X_1 \mid Y = k)f(X_2 \mid Y = k)\cdots f(X_d \mid Y = k)}{\sum_{i=1}^{K} P\{Y = i\}f(X_1 \mid Y = i)f(X_2 \mid Y = i)\cdots f(X_d \mid Y = i)} \qquad 3.10$$

By assigning d a value of 2, the equation is simplified into Equation 3.11.

$$P\{Y = X_1 \mid X_1, X_2\} = \frac{P\{Y = X_1\}f(X_1 \mid Y = X_1)f(X_2 \mid Y = X_1)}{P\{Y = X_1\}f(X_1 \mid Y = X_1)f(X_2 \mid Y = X_1) + P\{Y = X_2\}f(X_1 \mid Y = X_2)f(X_2 \mid Y = X_2)} \qquad 3.11$$

If $P\{Y=X_1|X_1, X_2\} > P\{Y=X_2|X_1, X_2\}$, then we can assign the new sample point Y to be of class X_1.

3.3.5 SCMV inoculation and ELISA detection

The SCMV virus isolate used (strain B of Maize dwarf mosaic virus [MDMV-B] designated Iowa 66-188 [ATCC-PV53]) was first isolated in Iowa in 1966 (Ford, et al., 1967; Hill, et al., 1973) and maintained in sweet corn (Zea mays L.' Golden Bantam'). Virus-infected leaf sap was prepared by grinding infected leaves in 50 mM (millimolar) of potassium phosphate buffer, pH 7.0. Mechanical inoculation of two leaf-stage sweet corn plants was done by rubbing leaf sap onto new leaves dusted with 600-mesh Carborundum (silicon carbide). Plants were maintained in a greenhouse room or a growth chamber at 20-22 °C with a photoperiod of 16 hours.

Enzyme-linked immunosorbent assay (ELISA) is a method applied to detection of SCMV. Leaf samples of SCMV-infected or mock-treated sweetcorn plants were collected for ELISA to detect infection by SCMV using the ELISA reagent set SRA18100 from Agdia. Assay was performed following the user guide of the product except for a 1-hour blocking step where 5% non-fat milk was added between the coating and sample dispensing steps. After adding the PNP substrate, the plate was incubated for 15-20 min and measured on a plate reader at 405 nm. Grinding buffer only was used as a negative control and the SCMV-infected sample used as inoculum was used as a positive control.

3.4 Results and Discussion

Four batches of corn plants were chosen as experiment objects. There were 20 maize plants in batches #1, #2, and #3, and 18 plants in batch #4. Batches #1, #2, #3 were grown in

one chamber; they are placed at left, middle and right positions within that chamber. 12 plants were inoculated by SCMV, 8 plants (mock) each were inoculated by water in batches #1, #2, and #3. 7 plants were inoculated by SCMV and 11 plants were inoculated by water in batch #4. The plants were inoculated 8 days after sprouting, and observation of the plants was begun 1 day after inoculation. The plants were tested every 3 days from the 1st day to the 25th day.

Each plant was placed in the working area of the system. After checking that the status of the ToF camera was set to "succeed", we began to test the plants. We first pressed the "Acquire 3D data" button and the system would capture 3D images of the plant in multi-views. The platform processed the data collected after "process 3D data" was triggered. When the process bar was at 100%, the corn plant model was reconstructed and displayed in a black window. After then pressing "compute parameter", a table displayed the phenotypic value of this plant, i.e., the lengths of each leaf and the stem height. The user next pressed "take color image", causing the arm to position the color camera and take a picture of the leaf center; the picture is displayed in a small window at the left side of the screen. The detection result, either "positive" or "negative", was displayed in the lower right window after triggering a "diagnose" button. At the lower right of the interface, there are two buttons: "Acquire" and "Gripping". They are used to locate the target leaf center and drive the robot hand to probe the target point.
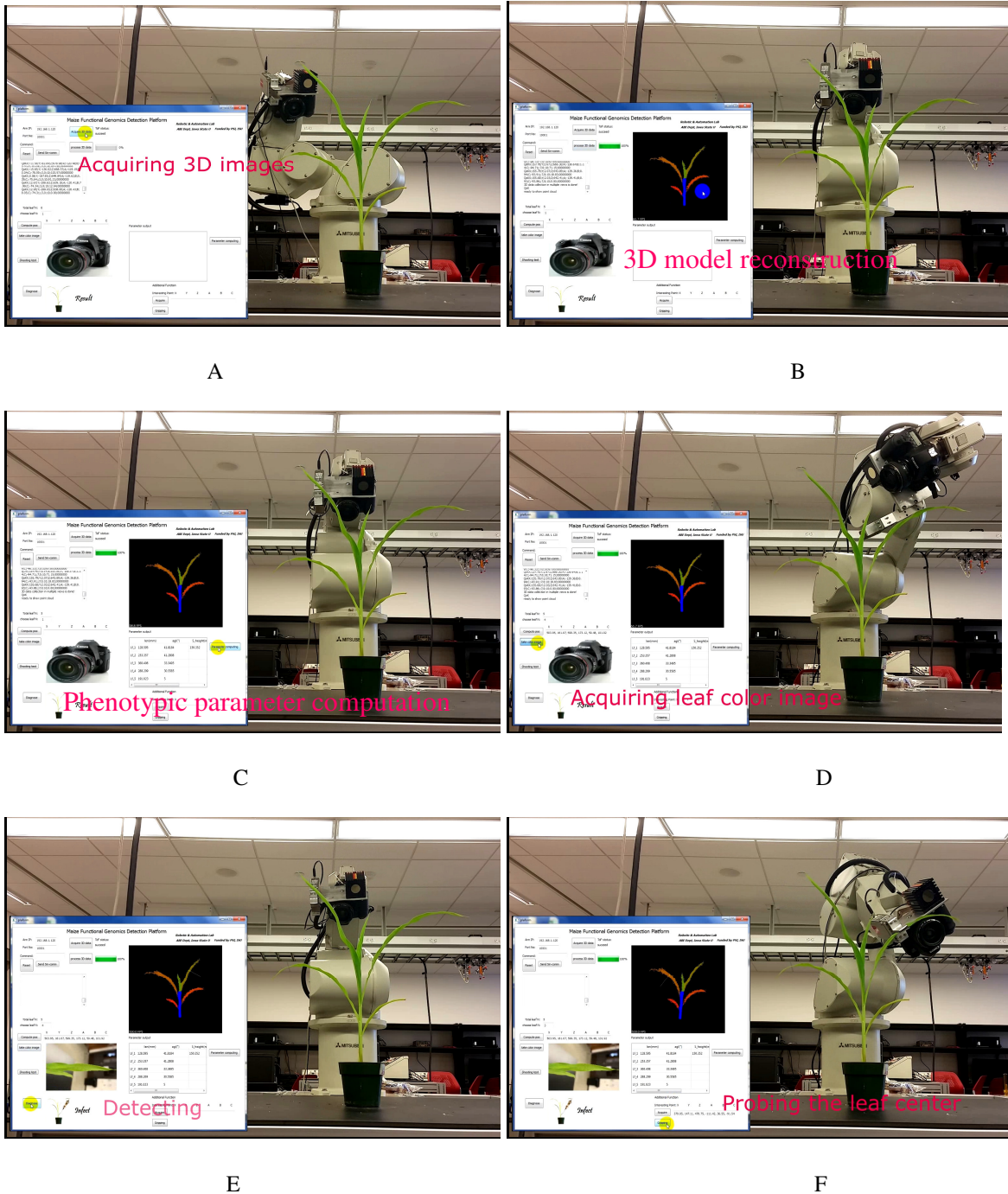
Figure 3.16. *System working flow map. A is the 3D image acquiring. B is the plant model visualization. C is plant parameter computing. D is acquiring leaf color image. E is diagnosing the infected plant. F is leaf probing.*

3.4.1 Detection of virus symptoms

The target leaves are the two leaves on top because the lower leaves are covered by upper leaves in the system view.

During each day when samples are taken, the system reports "positive" or "negative", where "positive" means the probability of "infected" is high and "negative" means the probability of "infected" is low for this plant. The leaf symptom pattern of an "infected plant" may be reported on different days than for other plants. For example, the pattern emerged about 1 week earlier for batch #4 than for batches #1, #2, and #3. On the 16th day, all 60 plants in batches #1, #2, and #3 tested "negative".

In batches #1, #2, and #3, plants 1 to 8 were inoculated by water and labeled as A, plants 9 to 20 were inoculated by virus reagent and labeled as B. The number "1" in the above table means "positive" while "0" means "negative". In batch #4, plants 1 to 7 were inoculated by and labeled as A, and plants 8 to 18 were inoculated by virus reagent and labeled as B. In the final result, we used the average of the 3 values to perform the classification. The final result of "diagnose" is shown in the table below.

One month after inoculation, all plants were sampled for ELISA to detect infection by SCMV. As shown in Figure 17, the negative control plants and all the mock-treated plants tested had a background OD405 less than 0.20, while the positive control and SCMV-infected plants had OD405 readings ranging from 1.27 to 1.92, significantly higher than the background readings. Ten SCMV-treated plants showed similar OD405 readings as the negative control plants, indicating unsuccessful SCMV infection. When leaf symptoms were checked to confirm infection, the result correlated well with the ELISA result. The ELISA result was treated as the gold standard in this project.
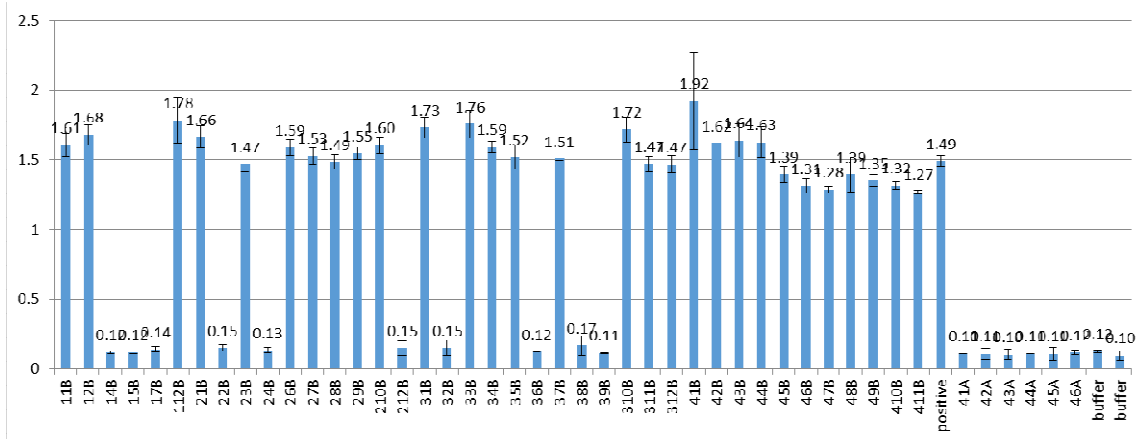
Figure 3.17. *ELISA result for 4 batches*

Table 3.1. Batch 1 (every sampling days) diagnose result

Plant ID	11A	12A	13A	14A	15A	16A	17A	18A	11B	12B	13B	14B	15B	16B	17B	18B	19B	110B	111B	112B
19 days	0	1	0	0	0	0	0	0	1	0	0	0	0	0	0	0	0	0	0	0
22 days	0	0	0	1	1	0	0	0	1	1	0	0	0	N/A	0	0	N/A	N/A	0	1
25 days	0	0	1	0	0	0	0	0	1	1	0	0	0	N/A	0	0	N/A	N/A	N/A	1

Table 3.2. Batch 2 (every sampling days) diagnose result

Plant ID	21A	22A	23A	24A	25A	26A	27A	28A	21B	22B	23B	24B	25B	26B	27B	28B	29B	210B	211B	212B
19 days	0	0	0	0	0	1	0	1	1	0	1	0	0	1	0	0	1	1	0	0
22 days	0	0	0	0	1	0	0	0	1	1	1	0	0	1	1	1	1	1	0	0
25 days	1	0	0	1	0	0	0	0	0	0	0	0	0	1	1	0	1	1	0	0

Table 3.3. Batch 3 (every sampling days) diagnose result

Plant ID	31A	32A	33A	34A	35A	36A	37A	38A	31B	32B	33B	34B	35B	36B	37B	38B	39B	310B	311B	312B
19 days	1	0	0	0	1	1	1	0	1	0	0	0	1	0	0	0	0	1	0	1
22 days	0	0	0	0	0	1	1	0	1	1	1	1	1	1	1	0	0	1	1	1
25 days	1	0	1	0	0	0	0	0	0	1	1	1	1	0	1	0	0	1	1	1

Table 3.4. Batch 4 (every sampling days) diagnose result

Plant ID	41A	42A	43A	44A	45A	46A	47A	41B	42B	43B	44B	45B	46B	47B	48B	49B	410B	311B
19 days	0	0	1	0	0	0	0	0	0	0	0	0	0	0	1	0	0	0
22 days	0	1	1	0	0	0	0	1	1	1	1	1	1	1	1	1	1	0
25 days	1	0	0	0	0	0	1	1	0	1	1	1	1	1	1	1	0	0

Table 3.5. *Batch 1 final diagnose result*

Plant ID	11A	12A	13A	14A	15A	16A	17A	18A	11B	12B	13B	14B	15B	16B	17B	18B	19B	110B	111B	112B
Diagnose	C	C	C	C	C	C	C	C	I	I	C	C	C	N/A	C	C	N/A	N/A	N/A	I
Truth	C'	C'	C'	C'	C'	C'	C'	C'	I'	I'	C'	C'	C'	N/A	C'	C'	N/A	N/A	N/A	I'
Correction	✓	✓	✓	✓	✓	✓	✓	✓	✓	✓	✓	✓	✓	N/A	✓	✓	N/A	N/A	N/A	✓

Table 3.6. *Batch 2 final diagnose result*

Plant ID	21A	22A	23A	24A	25A	26A	27A	28A	21B	22B	23B	24B	25B	26B	27B	28B	29B	210B	211B	212B
Diagnose	C	C	C	C	C	C	C	C	I	C	I	C	C	I	I	C	I	I	C	C
Truth	C'	C'	C'	C'	C'	C'	C'	C'	I'	C'	I'	C'	C'	I'	I'	I'	I'	I'	C'	C'
Correction	✓	✓	✓	✓	✓	✓	✓	✓	✓	✓	✓	✓	✓	✓	✓	✗	✓	✓	✓	✓

Table 3.7. *Batch 3 final diagnose result*

Plant ID	31A	32A	33A	34A	35A	36A	37A	38A	31B	32B	33B	34B	35B	36B	37B	38B	39B	310B	311B	312B
Diagnose	I	C	C	C	C	I	I	C	I	I	I	I	I	C	I	C	C	I	I	I
Truth	C'	C'	C'	C'	C'	C'	C'	C'	I'	C'	I'	I'	I'	C'	I'	C'	C'	I'	I'	I'
Correction	✗	✓	✓	✓	✓	✗	✗	✓	✓	✗	✓	✓	✓	✓	✓	✓	✓	✓	✓	✓

Table 3.8. *Batch 4 final diagnose result*

Plant ID	41A	42A	43A	44A	45A	46A	47A	41B	42B	43B	44B	45B	46B	47B	48B	49B	410B	311B
Diagnose	C	C	I	C	C	C	C	I	C	I	I	I	I	I	I	I	C	C
Truth	C'	C'	C'	C'	C'	C'	C'	I'	I'	I'	I'	I'	I'	I'	I'	I'	I'	I'
Correction	✓	✓	✗	✓	✓	✓	✓	✓	✗	✓	✓	✓	✓	✓	✓	✓	✗	✗

The first row in Tables 3.5, 3.6, 3.7 and 3.8 are the plant IDs; the second row is the diagnostic result from the system, where "C" means control plant and "I" means the infected plant. The third row presents ground-true from ELISA test, again with "C'" meaning control plant and the "I'" meaning infected plant. The last row shows the correction, where a check mark designates a correct result and a cross mark designates an incorrect result. In batches #1, #2, and #3, the system detected 18 "infected" plants in group B, while 3 plants were considered "infected" in group A. There were 74 cases, 65 correct and 9 incorrect, and the accuracy was 87.84%.

3.4.2 Leaf Probing test

We performed a leaf-probing test for batch#1 every sampling day. We tested for 2 directional errors: absolute error distance between gripper center and leaf center along the leaf midrib and the cross midrib.
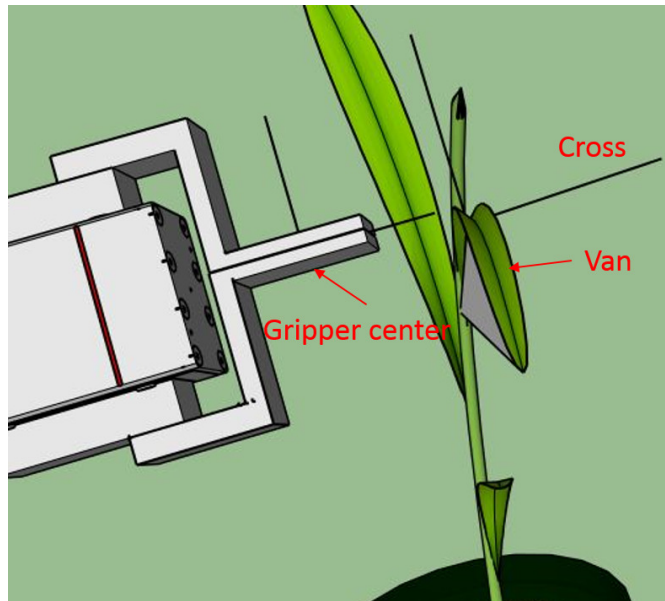
Figure 3.18. *Leaf Probing error definition.*
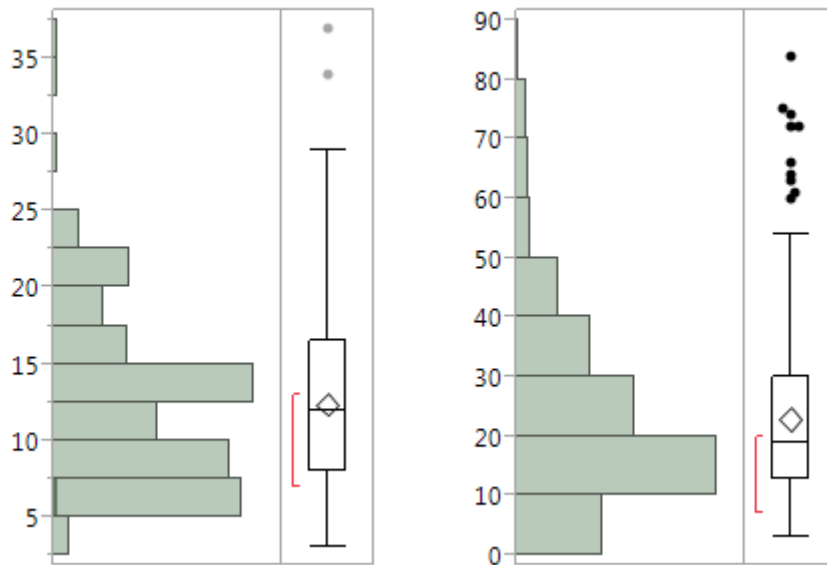
Figure 3.19. *Leaf Probing error distribution in cross direction (left) and along the midrib direction (right).*

Table 3.9. *Cross Midrib error (mm)*

	Quantiles			Summary Statistics	
100%	maximum	37	Mean		12.4041
75%	quartile	16.5	Std Dev		5.5868
50%	median	12	Std Err Mean		0.36062
25. %	quartile	8	Upper 95% Mean		13.1145
0%	minimum	3	Lower 95% Mean		11.6937
			N		240

Table 3.10. *Along Midrib error(mm)*

	Quantiles			Summary Statistics	
100%	maximum	84	Mean		23.0166
75%	quartile	30	Std Dev		15.2989
50%	median	19	Std Err Mean		0.9875
25. %	quartile	13	Upper 95% Mean		24.9621
0%	minimum	3	Lower 95% Mean		21.0713
			N		240

There were 240 leaves were tested. The mean of the error along the leaf midrib direction was 23 mm, and the median of the error was 19 mm. These two values across the midrib direction were 12.4 mm (mean) and 12 mm (median).

3.4.3 SCMV effects tests

We grew 60 maize plants, labeled as batches #1, #2, and #3. They were grown in one growth chamber and placed in the left (batch #1), middle (batch#2), and right (batch #3) chamber locations. There were 9 sampling days in the interval from the 1st day to the 25th day after the treatment. In each sampling day, the system would output the plant stem height, each leaf's length, for every plant. We also measured these parameters manually to provide a gold standard for comparison.

3.4.3.1 System result

According to the diagnostic result and plant parameter output, there were 216 plant-height values in the "control" group and 171 values in the "infected" group. We treated these 387 height values as observations, with effect factors that included Batch ID, plant ID, days of "infected or not". In this way we attempted to build a linear regression model.

$$Stem\_Height = Intecept + \beta_0 \times Days + \beta_1 \times Infected[Yes/No]$$

Because the testing of effect of "infected" status on plant height was the main activity of interest, we were concerned only about "days" and "infected" factors. We set an alpha level of 0.05, and used JMP 11 Pro software to run this model.

Table 3.11. Summary of fit (Height model using system output)

RSquare	0.7494
Root Mean Square Error	24.7232
Mean of Response	92.4383
Observations	378

Table 3.12. *Parameter estimates (Height model using system output)*

Term	Estimate	Std Error	t Ratio	Prob>|t|
Intercept	22.3892	6.2297	3.59	0.0468*
days	5.3986	0.1655	32.6	<.0001*
infected	-1.7401	-1.5096	16.19	0.2566
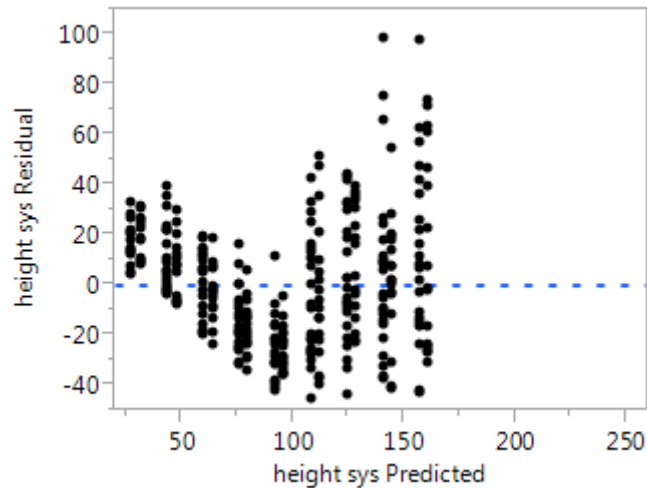
Figure 3.20. *Residual V.S. Predicted (Height model using system output)*

Table 3.11 shows that the R-square of this model is 0.7494. This means that there are 74.94 % samples in the population that can be explained using this model. The root mean square estimates the standard deviation of random error. 92.48 mm was the mean value of stem height and there were 378 samples observed in this model. Table 3.12 provides the coefficients of the factors and p-value forthe F-test. We can see the residula by predicted plot (Figure 3.20); there are obvious patterns, so this model is not suitable and should be changed. Beacause there are only 9 scales (day of 1, 4, 7, 10, 13, 16, 19, 22, 25) in the factor of "days", less than the response y of stem height (30 mm ~ 220 mm), we transferred the response y (stem height) to logarithmic representation. Here is the fixed model:

$$Log_e(Stem\_Height) = Intecept + \beta_0 \times Days + \beta_1 \times Infected[Yes \, / \, No]$$

Table 3.13. *Summary of fixed model fit (Height model using system output)*

RSquare	0.8067
Root Mean Square Error	0.2207
Mean of Response	4.4153
Observations	378

Table 3.14. *Parameter estimates of fixed model (Height model using system output)*

Term	Estimate	Std Error	t Ratio	Prob>|t|
Intercept	3.6653	0.0222	164.81	<.0001*
days	-0.0214	0.01147	-1.87	0.0621
infected	-0.0211	0.0579	0.0014	39.53

Table 3.15. *Effect test of Height fixed model (F-test)*

Source	Nparm	DF	F Ratio	Prob > F
days	1	1	1562.314	<.0001*
infected	1	1	3.5014	0.0621
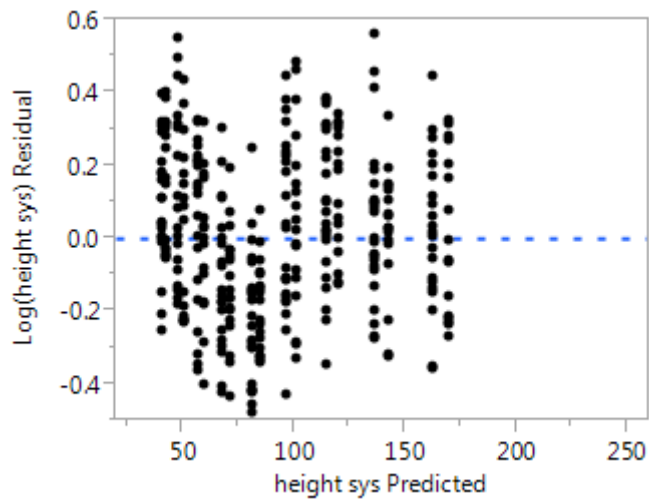
Figure 3.21. *Residual V.S. Predicted (Height fixed model using system output)*
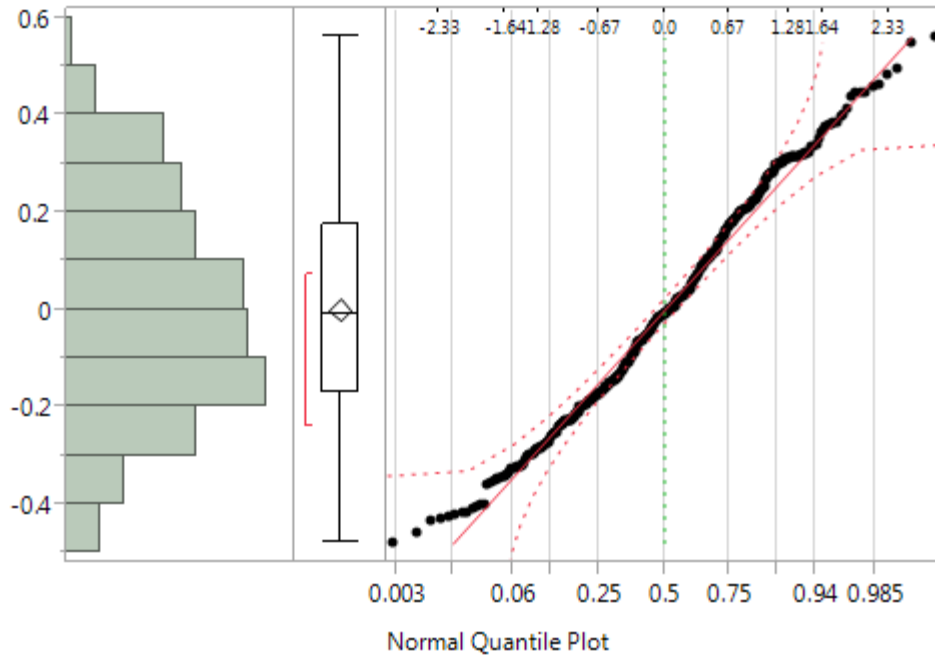
Figure 3.22 Quantile-Quantile Plot (Height fixed model using system output)

The R square is 0.8067, meaning that there are 80 % samples in the population that can be explained by this new model. The residula of the predicted plot (Figure 3.21) has no obvious pattern. The histogram and normal quantile plots (Figure 3.22) prove that the residual of the new model obeys a normal distribution. The new model thus is acceptable. The Effect Tests (F test) table shows that the P-values of "days" are very small and "infected" is larger than the alpha value. We fail to reject the hypothesis that the coefficient of "infected" is zero at α=0.05. For leaf length, we built a fixed model as below:

$$Log_e(Leaf\_length) = Intecept + \beta_0 \times Days + \beta_1 \times Infected[Yes / No]$$

*Table 3.16.* Summary of fixed model fit (Leaf length fixed model using system output)

RSquare	0.7026
Root Mean Square Error	0.3351
Mean of Response	5.0409
Observations	1455

Table 3.17. *Effect test of fixed leaf length fixed model using system output (F-test)*

Source	Nparm	DF	F Ratio	Prob > F
days	1	1	446.9407	<.0001*
Infected	1	1	2.6692	0.1228

The R-square of this model is 0.7, and the P-value of "days" is very small and "infected" is twice the alpha value. We thus fail to reject the hypothesis that the coefficient of "infected" is zero at α=0.05.

3.4.3.2 Ground-truth result

We use the ground-truth of stem height and leaf length and "diagnose" results to run the height and length model. The R-square of the height model and length model wer 0.88 and 0.73, the P-value of "Infected" were 0.1 and 0.22, i.e., greater than α = 0.05. We fail to reject the hypothesis that the coefficient of "infected" is zero at α=0.05.

Table 3.18. *Summary of fixed model fit (Height fixed model using manual measurement)*

RSquare	0.8803
Root Mean Square Error	0.1725
Mean of Response	4.4154
Observations	378

Table 3.19. *Effect test of fixed height fixed model using manual measurement (F-test)*

Source	Nparm	DF	F Ratio	Prob > F
days	1	1	2756.505	<.0001*
infected	1	1	2.7029	0.101

Table 3.20. *Summary of fixed model fit (Leaf length fixed model using manual measurement)*

RSquare	0.7301
Root Mean Square Error	0.3317
Mean of Response	5.011
Observations	1713

Table 3.21. Effect test of fixed leaf length fixed model using manual measurement (F-test)

Source	Nparm	DF	F Ratio	Prob > F
days	1	1	792.2429	<.0001*
Infected	1	1	1.6016	0.2252

In conclusion, there is no evidence to prove that SCMV would affect the maize plant with respect to stem height and leaf length during an interval ranging from 8 days to 32 days after sprouting.

3.4.4 Discussion and Conclusion

The results show that this platform is feasible for use in a maize-seeding phenotyping study. After distinguishing the infected plants, we used phenotypic parameters to build a model for analyzing the effects of "infected" on maize plants' stem height and leaf length. The P-values of "infected" were greater than $\alpha = 0.05$, so we concluded that the "infected" status does not affect the stem height and leaf length during V2~V5 growth stages. The probing test demonstrates that this system is able to approach the leaf center.

The infection detection error comes from four sources. The first factor is leaf texture image instability. We took a square sample from the leaf image center in this project, based on that assumption that an infected plant would have symptoms on its all its leaf surfaces. However, some symptoms emerged first at the bottom of the leaf and then appeared on the whole leaf after several additional days, so we misdiagnosed some infected plants as control plants in the early days of the test. A second source of error resulted from the classifier. It is easy to find a line to discriminate between the two classes, infected plants and control plants, in the training set, but when we have a large sample size, the overlap of these classes occurs and decreases the ability to discriminate. A third error source was the GLCM variables. While we used energy and homogeneity as judgmental factors, we could add more variables

and attempt to extract additional traits from the images to discriminate between these two

classes. A fourth error source was caused by biological issues. The training set cannot

include all symptoms and describe all control leaf patterns. It is probable that control leaves

may have irregular texture due to environment changes, and such situations are not included

in our training set.

In the future, using a more flexible robot arm and a better ToF camera with higher resolution

would be keys to improving system performance. It is necessary to take more than just one

center area of a leaf for sampling texture analysis. In addition to the GLCM, we can apply

other imaging methods to extract traits of the leaf surface. Different classifiers should be

tested and the training set should be enlarged. We might also optimize the algorithm and

apply more enhanced programing skills to increase the processing speed.

REFERENCES

Foundation, N. S., and G. Mcb. Phenomics: Genotype to Phenotype A report of the Phenomics workshop sponsored by the USDA and NSF, 2011.

Arvidsson, S.; Pérez-Rodríguez, P.; Mueller-Roeber, B. A growth phenotyping pipeline for arabidopsis thaliana integrating image analysis and rosette area modeling for robust quantification of genotype effects. New Phytol. 2011, 191, 895–907.

Li L, Zhang Q, Huang D. A Review of Imaging Techniques for Plant Phenotyping. Sensors. 2014; 14(11):20078-20111.

Azzari, G.; Goulden, M.L.; Rusu, R.B. Rapid characterization of vegetation structure with a Microsoft Kinect sensor. Sensors 2013, 13, 2384–2398.

Jin, J.; Tang, L. Corn plant sensing using real-time stereo vision. J. Field Robot. 2009, 26, 591–608.

Alenya, G., B. Dellen, and C. Torras. 2011. 3D modelling of leaves from color and ToF data for robotized plant measuring. In 2011 IEEE International Conference on Robotics and Automation. Shanghai, China: IEEE.

Nakarmi, A.; Tang, L. Automatic inter-plant spacing sensing at early growth stages using a 3D vision sensor. Computers and Electronics in Agriculture. 2012, 82, 23–31.

Song, Y.; Glasbey, C.A.; midrib der Heijden, G.W.; Polder, G.; Dieleman, J.A. Combining stereo and time-of-flight images with application to automatic plant phenotyping. In Image Analysis; Springer: Berlin/Heidelberg, Germany, 2011; pp. 467–478.

Shitala Prasad , Krishna Mohan Kudiri , R. C. Tripathi, Relative sub-image based features for leaf recognition using support vector machine, Proceedings of the 2011 International Conference on Communication, Computing & Security, February 12-14, 2011, Rourkela, Odisha, India

Zulkifli Bin Husin, Abdul Hallis Bin Abdul Aziz, Ali Yeon Bin Md Shakaff, Rohani Binti S Mohamed Farook, "Plant Chili Disease Detection Using The RGB Color Model", RNIS: Research Notes in Information and Service Sciences, 2013, Volume 13, pp. 78 ~ 83

Christian Wengert, Mireille Reeff, Philippe C. Cattin, Gábor Székely. "Fully Automatic Endoscope Calibration for Intraoperative Use" Bildverarbeitung für die Medizin Informatik aktuell 2006, pp 419-423

Radu Bogdan Rusu. (2009). Semantic 3D Object Maps for Everyday Manipulation in Human Living Environments. PhD dissertation, Technischen Universität München, Germany.

R. M. Haralick, K. Shanmugam and I. Dinstein "Textural features for Image Classification", IEEE Transactions on Systems, man and Cybernetics, Vol.3, pp. 610-621, November 1973.

De Moraes Frasson, R.P., Krajewski, W.F., 2010. Three-dimensional digital model of a maize plant. Agricultural and Forest Meteorology 150, pp. 478-488.

Ole Mathis Opstad Kruse, José Manuel Prats-Montalbán, Ulf Geir Indahl, Knut Kvaal, Alberto Ferrer, Cecilia Marie Futsaether, Pixel classification methods for identifying and quantifying leaf surface injury from digital images, Computers and Electronics in Agriculture, Volume 108, October 2014, Pages 155-165.

Kuo-Yi Huang, Application of artificial neural network for detecting Phalaenopsis seedling diseases using color and texture features, Computers and Electronics in Agriculture, Volume 57, Issue 1, May 2007, Pages 3-11.

CHAPTER 4. SUMMARY AND CONCLUSIONS

Summary

This project consisted of two main efforts, maize seeding phenotyping and determining the effects of "Infected" status on plant growth. To solve the first problem, I used a robot arm and a ToF camera as the main hardware set-up. The biggest challenge was achieving suitable communication between the robot arm and personal computer because of the need for real-time control. A protocol was applied for the communication function in which the robot arm functioned as a server and the computer functioned as a client. Commands to control the arm were transferred through a TCP/IP socket. After solving this problem, the next issue was how to build a user-friendly interface using a professional software approach. QT platform add-in Visual Studio 2010 was used as the programing environment. QT is a professional cross-platform application and UI development framework; it is very easy to draw windows and controls in the QT environment. Various libraries are implemented to support software development. PCL (Point Cloud Library) was applied to process 3D data, and some OpenCV functions were used to process color images. VTK (The Visualization Toolkit) helped in building the model visualization window.

The second problem was to analyze the "infected" factor in maize plants' growth. The first issue here is how to distinguish "infected" plants. Texture is the main difference between the control plant leaf and the infected plant leaf. The infected plant was inoculated with Sugarcane mosaic virus (SCMV); the texture of such a plant leaf exhibits irregular broken form, and I used the color and gray images to detect the infected leaf. The challenge was how to locate the target leaf. In my algorithm, I used 3D curves to fit the skeleton of the

leaf, find the normal to the leaf surface, and build a triangular surface to build the leaf center frame. In this way, the positional relationship between the arm and plant leaf were established. GLCM was applied to extract and digitize the difference between these two types of leaves. The next step was to classify them according to the digitized traits. Based on the phenotypic parameters and diagnostic results, I built the stem height and leaf length model and performed an effect test on the coefficient of the "infected" factor using JMP Pro 11.

Discussion and Conclusion

Errors in the phenotypic parameter measurement came from three sources: point cloud filters, ToF camera accuracy, and the leaf skeleton curve-fitting algorithm. The accuracy of the measurements are very sensitive to the filter parameters. Pass-through and outlier remover filters were used in this project, but since the performance of these filters depended on the plants' shapes, it was difficult to set filter parameters to satisfy all situations. If color information could be used to remove the noise and background from the plant images, that might decrease the measurement error. Such a color based-method might be implemented in different-shaped corn plants because the corn plants' color has merely difference.

Four sources contributed to infection-detection error. The first source was leaf texture image instability. In this project, we only took a square sample of the leaf image to analyze texture, but some symptoms of SCMV appeared first at the bottom of the leaf and then extended to the whole leaf only after several days. The infected plants were thus misdiagnosed as control plants in the early days of the test. The second source of error was

the classifier. In the training set, the two classes (infection and control plants) can be discriminated by a simple line. When the sample sizes become larger, the overlap of these classes occurs and decreases the classifier accuracy. Third, we used energy and homogeneity variables from the GLCM for trait extraction. More variables and traits from the leaf image could be used to discriminate between these two types of plants. Biological issues also can lead to error. The training set did not contain all symptoms of the SCVM or describe all control-leaf patterns. The control leaves probably have non-uniform texture because of the environment variations, but our training set did not consider these situations.

This platform has the capacity for reconstructing a 3D model of maize plant during V2~V5 growth stages, acquiring the phenotypic parameters, and distinguishing between "infected" and "control" plants. There is no evidence to show that the "Infected" factor affects the maize plants with respect to stem height and leaf length during V2~V5 stages, according to the models.

In the future, we can improve the platform's performance by optimizing the segmentation algorithm. If we wish the system to work on a wider range of maize growth stages and to process more than one plant at a time, a more flexible robot arm and improved ToF camera with higher resolution would be necessary.